



HAL
open science

Experimental study of thermally enhanced recovery of high-viscosity DNAPL in saturated porous media under non-isothermal conditions

Nicolas Philippe, Hossein Davarzani, Stéfán Colombano, Malorie Dierick, Pierre-Yves Klein, Manuel Marcoux

► **To cite this version:**

Nicolas Philippe, Hossein Davarzani, Stéfán Colombano, Malorie Dierick, Pierre-Yves Klein, et al.. Experimental study of thermally enhanced recovery of high-viscosity DNAPL in saturated porous media under non-isothermal conditions. *Journal of Contaminant Hydrology*, 2021, 243, pp.103861. 10.1016/j.jconhyd.2021.103861 . hal-03745454

HAL Id: hal-03745454

<https://brgm.hal.science/hal-03745454v1>

Submitted on 22 Aug 2023

HAL is a multi-disciplinary open access archive for the deposit and dissemination of scientific research documents, whether they are published or not. The documents may come from teaching and research institutions in France or abroad, or from public or private research centers.

L'archive ouverte pluridisciplinaire **HAL**, est destinée au dépôt et à la diffusion de documents scientifiques de niveau recherche, publiés ou non, émanant des établissements d'enseignement et de recherche français ou étrangers, des laboratoires publics ou privés.



Distributed under a Creative Commons Attribution - NonCommercial 4.0 International License

Experimental study of thermally enhanced recovery of high-viscosity DNAPL in saturated porous media under non-isothermal conditions

Nicolas Philippe^{a,c}, Hossein Davarzani^a, Stéfan Colombano^a, Malorie Dierick^c, Pierre-Yves Klein^c,
Manuel Marcoux^b

^a*BRGM (French Geological Survey), 3 avenue Claude Guillemin, 45100 Orléans, France*

^b*Institut de Mécanique des Fluides de Toulouse (IMFT), Université de Toulouse, CNRS, 31400 Toulouse, France*

^c*REMEA, 22-24 rue Lavoisier, 92000 Nanterre, France*

1. Introduction

The remediation of sites contaminated by dense non-aqueous phase liquid (DNAPL) remains an open subject. These phases are composed of substances that are generally toxic and carcinogenic. Among DNAPLs are coal tars with complex liquid phases. They are composed of monocyclic and polycyclic aromatic hydrocarbons (PAHs) as well as phenolic compounds (Lee et al., 1992). Previous characterization studies have shown that coal tars vary according to origin. The coal tar used in this study is the same as the one studied recently by (Johansson et al., 2019; Iravani et al., 2020; Philippe et al., 2020).

Pump and treat technology remains the most widely used to remediate high-saturation coal tar sources. In general, remediation efficiency is very low for DNAPLs, and this method is technologically and economically unsatisfactory (USEPA, 1996; Russell and Rabideau, 2000; Kavanaugh and Kresic, 2008; Navy, 2008; Newell et al., 2011). This low efficiency flows from a combination of factors: (i) Coal tar is denser than water: it flows along the most permeable local paths, often in the form of fingerings, to impermeable horizons, and then forms deep source zones; (ii) When recovering coal tar by pumping, the unfavorable viscosity ratio causes water to infiltrate in the form of fingerings. These fingers gradually trap significant volumes of coal tar, until the water starts to be recovered from the pumping well. At this stage, only a tiny amount (often mixed in water) of coal tar is collected that no longer allows the soil to be decontaminated; (iii) Some coal tars have non-Newtonian behavior (Fitzer et al., 1987) but the coal tar used in this study showed Newtonian behavior (Philippe et al., 2020).

Thermal desorption techniques have already proved their effectiveness for the remediation of DNAPL-contaminated soils. Heat treatment can be highly effective for volatile organic compounds (VOCs), with efficiencies of up to 99%, even in highly contaminated sources (Renoldi et al., 2003; Johnsen et al., 2005). For example, Heron et al. (1998) succeeded in extracting 99.8% of TCE from a silty soil 50 cm deep using this method (Heron et al., 1998). Recently, the same type of process was applied to PAH-contaminated sites with an equally efficient yield by reaching soil temperatures of 325°C (Baker et al., 2006). Nevertheless, this technique has a significant financial cost because of the high energy required (McDade et al., 2005; Baston et al., 2010). Another technique, quite similar, consists in burning the pollutant when it is flammable, which happens to be the case of coal tar. The smoldering fire provoked during this combustion can incinerate coal tar source zones with yields as high as thermal desorption techniques in unsaturated zones (Switzer et al., 2009; Hasan et al., 2015). Nowadays, this technique has already been applied to coal tar in the field, with a mass concentration of PAHs decreased by 97% (Scholes et al., 2015). Smoldering fire is, however, a type of combustion whose fundamental understanding is still limited, and whose environmental impact on the soil has not yet been studied

(Rein, 2009). However, these techniques generate temperatures higher than 100 °C (boiling temperature of water). On the contrary, here, thermally enhanced DNAPL recovery focuses on temperatures lower than 100 °C to avoid contaminant evaporation. The goal is to reduce the quantity of residual DNAPL formed during pumping that could require further treatment or management.

We are interested in the pumping of coal tars and the means of recovering a larger quantity of contaminants. Therefore, the objective is to increase the recovery rate. By reducing fingerings, as little coal tar as possible is trapped during pumping. A similar problem has already been faced in petroleum engineering, in relation to the recovery of heavy oils. The most appropriate solution is to heat the medium and the liquids, to reduce the fluid-fluid viscosity ratios (Koci et al., 1989; Wang et al., 2006). Most tests in petroleum engineering demonstrate the effectiveness of heating and its feasibility at the laboratory scale whether by external heating or by injecting hot water. However, they represent an essentially one-dimensional flow in a horizontal or vertical column and do not consider the 2D flow complexity of a real pollution under non-isothermal conditions.

The change of dimension from 1D columns to a 2D-tank scale is a recent subject of study on DNAPL. Wilking et al. (2013) followed the infiltration and dissolution of a DNAPL (trichloroacetic acid) and obtained saturation fields using X-ray tomography technology (Wilking et al., 2013). More recently, DNAPL saturation has been monitored in transparent media thanks to a calibration between the optical density and the DNAPL volume fraction. These techniques are referred to as the light reflection method (LRM) and light transmission method (LTM). For instance, Alazaiza et al. (2016) used LRM to monitor progressive infiltration of PCE (Alazaiza et al., 2016). (Darnault et al., 1998) similarly followed the oil/water system using a blue dye with LTM (Darnault et al., 1998). (Heiderscheidt et al., 2008) also used LTM to study in situ oxidation on sand impacted by PCE (Heiderscheidt et al., 2008). Colombano et al. (2020) demonstrated that from LRM, the residual saturation of chlorinated solvents in 2D-tank pumping experiments could be estimated with good accuracy ($R^2 = 0.95$).

Monitoring by imaging allows the study of transient phenomena linked to DNAPL flows in porous media. (Colombano et al., 2021), for example, explored the remediation of chlorinated solvents by increasing the system's temperature and chemical enhancement using surfactants in 0.1 mm and 0.5 mm glass beads (Colombano et al., 2021). No temperature effect has been reported in this study as their DNAPL's dynamic viscosity and surface tension did not vary with temperature. However, coal tars are much more viscous than most DNAPLs, including chlorinated solvents. Moreover, coal tars' dynamic viscosity decreases greatly with temperature (Philippe et al., 2020). Also, (Colombano et al., 2021) only worked in isothermal conditions. Their recovery by pumping can therefore change the observed results (Pankow and Cherry, 1996; Li and Schwartz, 2004; Childs et al., 2006). Moreover,

thermal techniques for soil remediation have also already been studied on this scale. Heat transfers in a small-scale two-dimensional experimental tank (60 cm × 45 cm × 1 cm) filled with 0.5 mm glass beads and a large-scale tank (2.4 m × 1.2 m × 0.15 m) filled with sandy soil have been investigated by (Krol et al., 2011). Furthermore, (Johnson et al., 2011) studied the potential of the electrical resistance heating (ERH) technique at low temperature (30–50 °C) to enhance the clean-up of TCE and PCE sources in the same large-scale tank (Johnson et al., 2011). The authors concluded that pre-heating groundwater and a TCE or PCE source is an efficient way of promoting its recovery in highly permeable media. Also, the generated heat can enhance in situ biodegradation or chemical reactions afterward. However, no existing study considers the transient temperature and saturation variations together during the pumping of a high-viscosity fluid in highly permeable porous media, which is the main goal of our study.

The coal tar used here comes from a seriously polluted site in France. Due to its characteristics, this coal tar is not compatible with imaging techniques. It sticks on the glass walls and is completely opaque to the light of the visible spectrum. Thus, we conducted most of our studies using the canola oil/ethanol model pair proposed by Philippe et al., 2020. Its properties were recently approved in (Philippe et al., 2020) as well as the reduced residual saturation with increased temperature. The presence of viscous fingering generated due to the dynamic effect (as opposed to static experiments) was found to be responsible for the high residual saturation in the system. Increasing the temperature reduces viscous fingering and increases ethanol film presence. Residual oil saturation falls as a consequence (Philippe et al., 2020).

In two-phase flow in porous media, viscous fingering may appear when the viscosity ratio M is unfavorable (<1) and the velocity in the experiment is higher than a critical velocity U_c , where M and U_c are defined as (Lenormand et al., 1988; Glass and Nicholl, 1996):

$$M = \frac{\mu_{inv}}{\mu_{dis}}, \quad (1)$$

$$U_c = \frac{|\rho_{inv} - \rho_{dis}|gK}{\phi|\mu_{inv} - \mu_{dis}|}, \quad (2)$$

where μ_{inv} (Pa.s) and ρ_{inv} (kg.m⁻³) are the dynamic viscosity and density of the invading phase, μ_{dis} (Pa.s) and ρ_{dis} (kg.m⁻³) the dynamic viscosity and density of the displaced phase. K (m²) is the permeability of the porous medium and ϕ (-) its porosity. g (9.8 m.s⁻²) is the conventional value of gravitational acceleration.

We investigated the presence of viscous fingering and how that influences the shape of the cone of depression, as well as the residual saturation. The experimental development and most of the conclusions were obtained on the oil/ethanol liquid pair. The coal tar/water pair was also studied as an industrial application.

Our main objective was to study the coupling between temperature and immiscible two-phase flow in pumping conditions. The porous medium consists of homogeneous glass beads with high permeability to avoid any other disturbing phenomena. First, the experiments were carried out on the oil/ethanol pair to work with simple fluids whose properties are well known, and which allow optical monitoring. Then the pumping of DNAPL in the saturated zone was carried out as an industrial application to observe similarities between two pairs of immiscible fluids.

In practice, during these experiments, the saturation (S) was followed by time-domain reflectometry (TDR, local small volumes) and imaging (2D fields). The temperature (T) was followed using thermocouples. We focused on: (i) the shape of the line delimiting the two continuous phases, that referred to as the “interface” and represented by a pumping cone (cone of depression), (ii) the saturation during pumping and the residual saturation after pumping, (iii) the frequency and appearance of the fingerings encountered, and (iv) the recovery rates and volumes.

2. Experimental setup and procedures

2.1. Experimental setup

The experimental setup consists of a decametric 2D tank, with a pump, a camera, and a well instrumented monitoring system. Wetting and non-wetting phases are injected into the same 1 mm homogeneous glass beads used in (Philippe et al., 2020) and pumped under isothermal (circulation of cold or hot water around 2D tank) and non-isothermal (heating element) conditions. The mean porosity φ and permeability K of the glass beads used are 0.4 and $3.5 \times 10^{-10} \text{ m}^2$, respectively. Saturation and temperature were monitored during the heating and pumping steps (Figure 1).

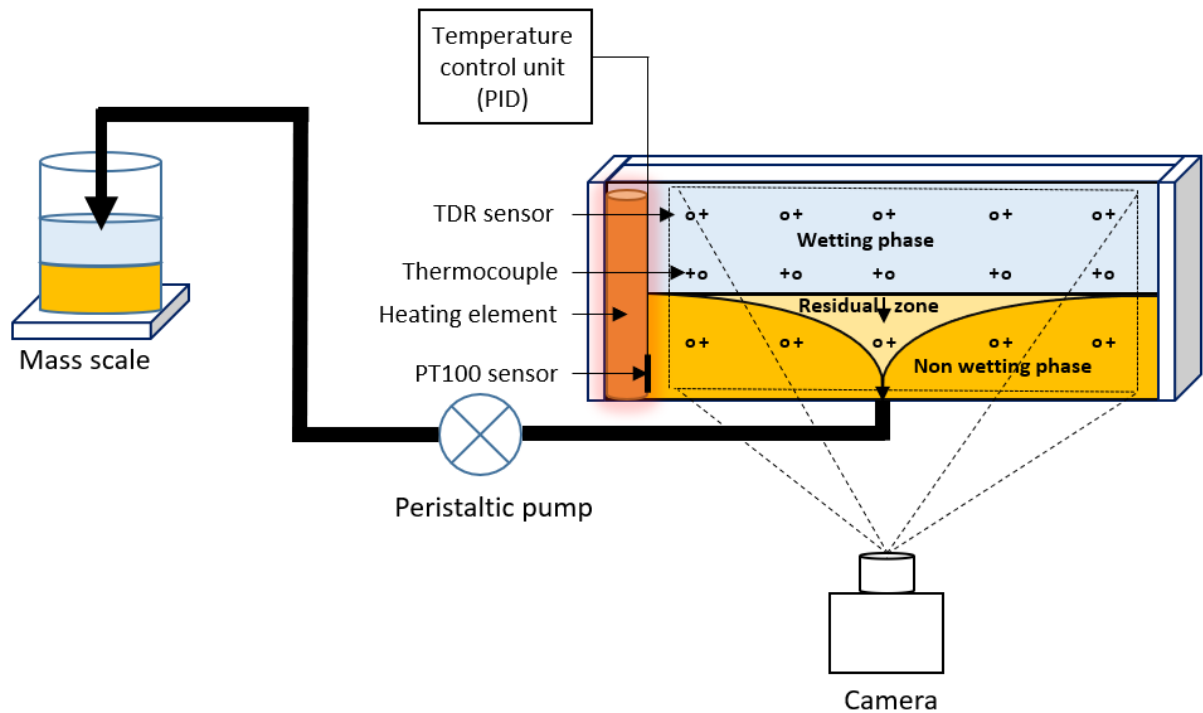


Figure 1 Schematic of the experimental setup

The 2D tank (height = 30 cm, width = 50 cm, thickness = 7 cm) made of polyvinylidene fluoride (PVDF), fabricated by SCODIP®, was used to carry out all the pumping experiments (Figure 2). The front of the tank is transparent (glass 1 cm thick) so that the environment can be photographed at different times. Photographs are taken to obtain saturation fields during the pumping experiments. The apparatus consists of a central reservoir containing the porous medium, and side channels (counter channels) regulating the static levels of the liquids used. The counter-channels are connected to the central reservoir by a metal grid which allows fluids to pass but blocks the glass beads inside the central reservoir. Side and bottom accesses allow connection of pipes and injection or pumping of liquids. The internal diameter of the pumping access points is 3.125 cm. The tank is equipped with a double jacket in back part and double-glazing in front allowing experiments to be carried out in isothermal conditions by circulating regulated temperature water using a thermostatic bath (LAUDA, model ECO RE 420). Heated water circulates through the double-jacket and double-glazing to keep the temperature steady during isothermal experiments.

A heating element (350 W , 0.7 W.cm^{-2}) made of stainless steel and designed by Vulcanic®, is added inside the tank near its left wall cavity to create non-isothermal heating conditions. In a real case, heating is not uniform due to the size of the field. The heating element is used to reproduce more realistic conditions that correspond to non-isothermal pumping. This element is helical, 30 cm long and 6.5 cm in diameter. The element heats the porous medium uniformly along the x -axis. The heating is regulated by a proportional–integral–derivative controller (PID controller), using a control box and a

PT100 probe connected to the heating element (Figure 1). Even if the heating element is not needed for the isothermal case, it is kept inside the tank for all the experiments to ensure the same conditions between isothermal and non-isothermal conditions. The double-jacket and double-glazing systems, which have been filled with air for non-isothermal cases, can communicate freely with the air of the experiment room through the inlet and systems. This reduces significantly the heat loss from the 2D tank front glass and back parts.

Pumping used a peristaltic pump (Watson Marlow 530 U). The liquids recovered are injected directly into a beaker placed on a precision balance (Sartorius Cubis MSE ± 0.1 mg). Acquisition of the recovered mass is automatic and performed every 6 seconds.

We used LRM based on image analysis to obtain a precise relationship between light intensity and saturation field to determine the average DNAPL saturation inside the tank. A 34-megapixel (7360 \times 4912) Nikon® D810 digital still camera with a NIKKOR 105 lens and two 500W Broncolor® projectors were used. Projectors prevented light reflection and shadow and improved the brightness of photographs. The imaging system was installed in a dark room to prevent outside light from influencing the brightness of the photographs.

The tank was also equipped with 15 measuring units consisting of TDR probes (5TE, Meter Group®) to measure the medium relative permittivity and type K thermocouples at the back of the tank (provided by TC S.A.® precision $\pm 0.4\%$, sensitivity 0.150 s). The position of these sensors is shown in Figure 2 and represents a network of three rows and five columns. A Campbell® CR-1000 datalogger was used to acquire temperature and relative permittivity measurements. In practice, TDRs 11, 21, and 31 were removed, as well as thermocouple 21, because they were physically blocked by the addition of the heating element.

The diameter of the pumping access point (3.125 cm) is around half of the 2D tank thickness (7 cm). The saturation fields obtained with LRM are just representative of the saturation on a 2D plane corresponding to the front glass wall of the tank. We effectively observed that the wetting phase (water or ethanol) flows out of the tank, while the apex of the cone of depression does not still reach the pumping point. This is evidence of a very small 3D effect near the pumping point. The difference between the recovered fluid mass using the mass scale and imaging at the end of the experiment proves also this small 3D effect. Therefore, the saturation obtained with LRM will be compared to saturation measured from TDR probes to evaluate the two measuring methods. The comparison between both techniques is used to determine potential 3D effects that cannot be captured by the LRM technique.

The liquid pairs used to carry out these experiments are the same as Philippe et al., 2020:

- the coal tar/water pair representing in a geometrically simplified manner a layer of DNAPL on an impermeable substratum in an aquifer. The “sticky” aspect and the lack of transparency of the coal tar are nevertheless two properties that complicate its study. The water used was previously degassed to avoid the presence of residual air in the tank.

- the canola oil/ethanol pair serves as a “model” pair. Sodium chloride was also dissolved in ethanol (0.65 g/L) to make measuring electrical resistivity easier in a parallel work (Iravani et al., 2020).

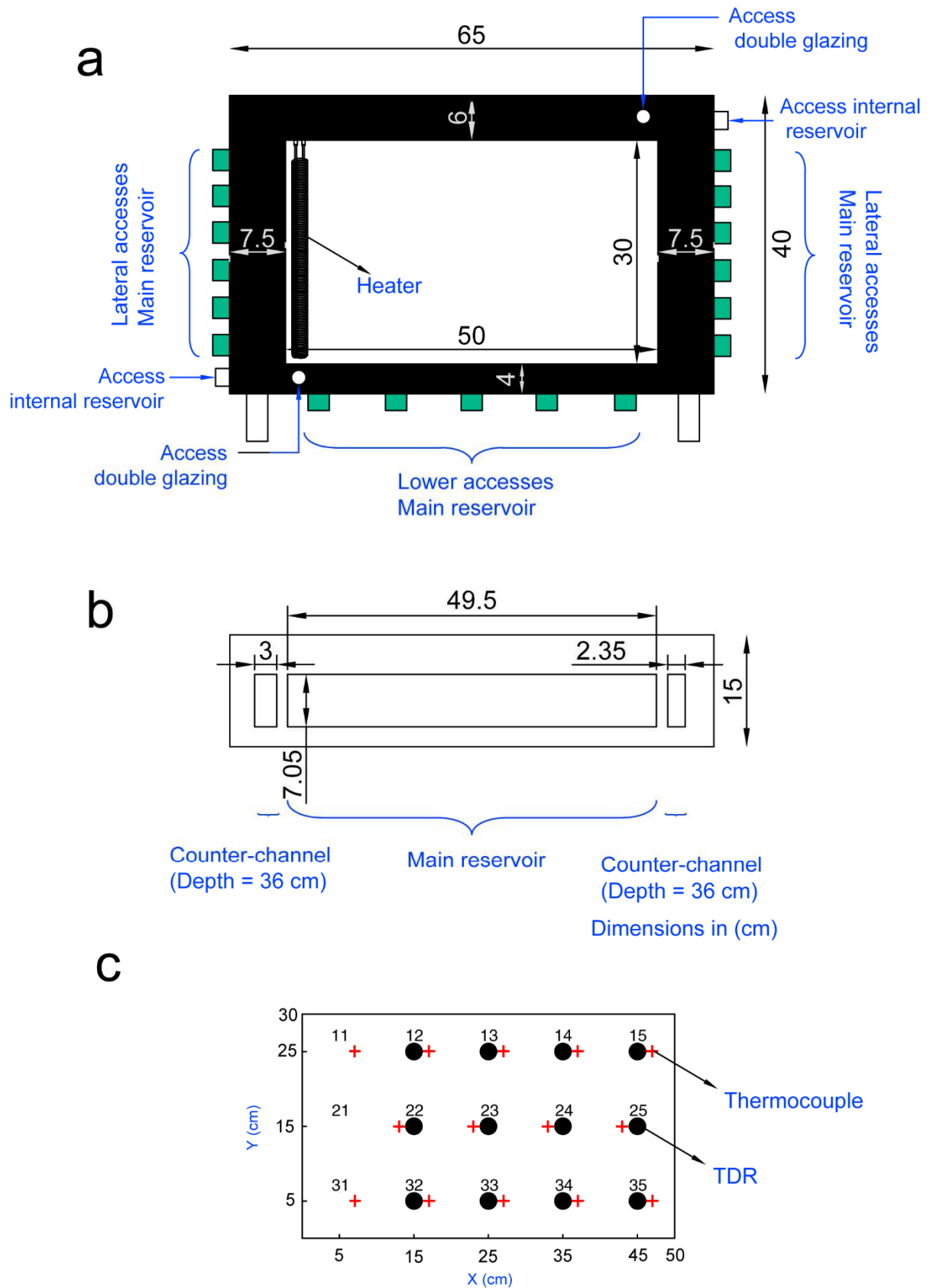


Figure 2 Schematic layout of the a) front, b) top and c) front of the 2D tank with the position of the TDR sensors.

2.2. Fluid properties

The density and the dynamic viscosity of each fluid are specified in Table 1 for the coal tar (CT) / water (W) pair and Table 2 for the canola oil (O) / ethanol (E) pair (Philippe et al., 2020). The measured interfacial tension and the contact angle are also presented. We used the pendant drop technique to measure interfacial tension of the fluids by forming a drop of coal tar (or oil) in a small cuvette filled with degassed water (or ethanol). Contact angles were measured using the sessile-drop method by placing a drop of coal tar (or oil) on the bottom plate of the same quartz glass cuvette previously filled with degassed water (or ethanol). The low interfacial tension of coal tar/water can be related to the presence of amphiphilic substances in the coal tar sampled from a real site. Barranco and Dawson (1999) reported similar low values of interfacial tension of coal tar-water at basic pH values (pH > 9). Sanaiotti et al. (2010) also reported interfacial tension values between 1-3 mN.m⁻¹ for soybean oil and water and ethanol mixtures (Sanaiotti et al., 2010). The high (> 90°) values reported of contact angle indicate that coal tar and oil are the non-wetting fluids. Properties and trends of these liquid pairs are similar, which supports the use of the canola oil and ethanol pair to model coal-tar and water two-phase flow.

Table 1 Density (ρ), dynamic viscosity (μ), interfacial tension (γ), and contact angle on a glass slide (θ) of the coal tar (CT)/water (w) fluid pair

T (°C)	ρ_{CT} (kg.m ⁻³)	ρ_W (kg.m ⁻³)	μ_{CT} (Pa.s)	μ_W (Pa.s)	$\gamma_{CT/W}$ (mN.m ⁻¹)	$\theta_{CT/W}$ (°)
10	1101	999.4	8.62×10^{-2}	1.28×10^{-3}	2.37	129
20	1096	996.8	5.09×10^{-2}	9.99×10^{-4}	2.34	127
30	1091	994.2	3.11×10^{-2}	7.95×10^{-4}	2.30	127
40	1086	991.6	1.96×10^{-2}	6.42×10^{-4}	2.27	126
50	1081	989.0	1.27×10^{-2}	5.25×10^{-4}	2.23	124

Table 2 Density (ρ), dynamic viscosity (μ), interfacial tension (γ), and contact angle measured on a glass slide (θ) of the oil (O)/ethanol (E) fluid pair

T (°C)	ρ_O (kg.m ⁻³)	ρ_E (kg.m ⁻³)	μ_O (Pa.s)	μ_E (Pa.s)	$\gamma_{O/E}$ (mN.m ⁻¹)	$\theta_{O/E}$ (°)
10	916	814	1.90×10^{-1}	2.51×10^{-3}	2.30	134
20	911	807	1.18×10^{-1}	1.93×10^{-3}	2.18	137
30	906	801	7.54×10^{-2}	1.52×10^{-3}	2.06	141
40	901	795	4.97×10^{-2}	1.21×10^{-3}	1.94	126
50	896	789	3.36×10^{-2}	9.76×10^{-4}	1.82	130

2.3. Experimental procedures

2.3.1. Setup preparation and heating

The heating element was first installed on the left side of the empty tank and initially held straight with a support. Oil was injected through the five lower inlets using a low flow peristaltic pump simultaneously ($10 \text{ mL}\cdot\text{min}^{-1}$) to an initial height of 1.5 cm. From this moment, glass beads were progressively added while continuing the oil injection. The glass beads were also stirred during injection to homogenize their distribution in the tank. The injection and addition were done slowly to avoid any air trapping during this step. The oil level was always kept just above the level of the glass beads to also prevent air trapping. Oil injection stopped when the oil reached a height of 15 cm. Then ethanol was injected in the same way using the lateral counter-channels from above. The ethanol injection stopped when the tank was fully saturated (all 30 cm). During the injection of the liquids, precautions were taken to avoid mixing the oil and ethanol, and to keep the interface between both liquids at 15 cm as straight as possible (Figure 1).

Initially, in the case of oil/ethanol, the oil completely saturates the porous medium from 0 to 15 cm and the same for ethanol from 15 to 30 cm. However, in the case of the coal tar/water application case, the tank preparation described above was slightly changed. The 2D tank was first fully saturated with water. Then, coal tar was injected through the five lower inlets to perform primary drainage up to a height of 15 cm. This was done to better represent a real pollution case, which is rarely fully saturated. In addition, preparing the experiment with coal tar required more attention. As a first step, the solid particles contained in the coal tar were removed using a glass fiber filter (GF/D, pore size $2.7 \mu\text{m}$). Water present in the collected coal tar during sampling was also removed using a vacuum pump and a $10 \mu\text{m}$ hydrophobic membrane.

For both liquid pairs, once the tank was full, the initial relative permittivity measurements were carried out for 12 hours to verify that the TDRs were working correctly. Initially, the tank was at room temperature ($20 \text{ }^\circ\text{C}$). In the case of pumping under isothermal conditions, a temperature-controlled water bath was used to set the tank temperature to $20 \text{ }^\circ\text{C}$ or $35 \text{ }^\circ\text{C}$. The heating element was still added in isothermal cases so that the porosity was the same as in non-isothermal experiments. In non-isothermal conditions, the temperature of the heating element was set to $60 \text{ }^\circ\text{C}$ with the temperature control unit (PID controller). The tank was heated until a steady state was reached (this step lasts about 8 hours). During the heating phase, the temperature of the tank and the permittivity values were measured with sensors directly in contact with the porous medium inside the tank.

2.3.2. Pumping procedures

Pumping used a flexible tube (diameter 3.125 mm) located on the lower central inlet of the tank. The rotation speed was fixed at 84.3 rpm or 25 rpm. The corresponding pumping rates (Q) of these rotations, for water and ethanol, were $100 \text{ mL}\cdot\text{min}^{-1}$ and $20 \text{ mL}\cdot\text{min}^{-1}$, respectively. The measured pumping rate for the same rotation rates but for canola oil was lower than water and ethanol at 84.3 rpm ($70 \text{ mL}\cdot\text{min}^{-1}$) and the same at 25 rpm ($20 \text{ mL}\cdot\text{min}^{-1}$). The mass of recovered liquid was measured continuously with an automatic acquisition mass balance every 6 seconds. The time at which the ethanol begins to be recovered was also noted and is defined as the breakthrough time.

Photographs of the tank were taken using the light reflection method (LRM) technique during the pumping step. Raw images and data were saved in Nikon format every three minutes at $100 \text{ mL}\cdot\text{min}^{-1}$ and 5 minutes at $20 \text{ mL}\cdot\text{min}^{-1}$. The pumping step lasted until the stationary state was reached, which was indicated by the exclusive recovery of the wetting phase (ethanol or water), and a stationary depression cone. The photographs were then converted into TIFF format with Capture One® software. The images were finally processed with the open-source software Fiji to calibrate light intensity and saturation according to the method developed by (Colombano et al., 2021) and (Philippe et al., 2020). All of our experiments are summarized in Table 3.

Table 3 Summary of pumping experiments

Experiment number	Liquids	Condition	Flow rate, Q ($\text{mL}\cdot\text{min}^{-1}$)	Initial temperature of 2D tank ($^{\circ}\text{C}$)	Setpoint temperature ($^{\circ}\text{C}$)
1	O/E	Isothermal	100	20	N/A
2	O/E	Isothermal	100	32	N/A
3	O/E	Non-isothermal	20	20	60
4	O/E	Non-isothermal	100	20	60
5	CT/W	Isothermal	100	20	N/A
6	CT/W	Non-isothermal	100	20	60

In addition to the viscosity ratio (M), the Capillary number (Ca) and Bond number (Bo), both of which have an important role in analyzing the behavior of fluids in porous media, can be calculated using the fluid velocity at the pumping point ($U_p = 2.88 \times 10^{-4} \text{ m/s}$) and solid particle size (ℓ) to generalize our experimental conditions.

$$Ca = \frac{U_p \mu_{inv}}{\gamma}, \quad Bo = \frac{(\rho_{dis} - \rho_{inv}) g \ell^2}{\gamma}, \quad (3)$$

The calculated dimensionless numbers are listed in Table 4 Dimensionless numbers for different isothermal pumping scenarios ($Q=100 \text{ mL/min}$) and for two temperatures and fluid pairs. Heating

increases the viscosity ratio by 30% but has no significant effect on Capillary numbers which are low because of the low pumping flow rate. The Bond numbers are slightly less than one. Heating or changing the fluids pair do not impact significantly the Bond number.

Table 4 Dimensionless numbers for different isothermal pumping scenarios ($Q=100$ mL/min)

Experiment number	M	Ca	Bo
1	1.64×10^{-2}	2.55×10^{-4}	4.66×10^{-1}
2	2.18×10^{-2}	2.12×10^{-4}	4.13×10^{-1}
5	1.96×10^{-2}	1.23×10^{-4}	4.16×10^{-1}

3. Image analysis and sensor calibrations

3.1. Image analysis

Both the light transmission method (LTM) and light reflection method (LRM) have been used in previous studies on the visualization of two-phase flow in porous media (Geel and Sykes, 1994; Darnault et al., 1998; Wu et al., 2017). The main idea is to determine a relationship between light intensity and wetting phase saturation. Previous works have shown that there is a logarithmic relationship between light intensity and saturation (Tidwell and Glass, 1994; Gerhard and Kueper, 2003; Colombano et al., 2020). In that research, the optical density OD is defined such that $OD = \log\left(\frac{I_{mes}}{I_0}\right)$ where I_{mes} is the measured intensity and I_0 is the white intensity to obtain a linear relationship between optical density and wetting phase saturation. In the case of coal tar and oil, the optical density was measured for uniform saturation values ($S_w = \{0; S_{r,w}; S_{r,nw}; 1\}$) to get the line coefficients (Figure 3), where S_w is the wetting saturation, $S_{r,w}$ and $S_{r,nw}$ irreducible and residual saturation, respectively. A small drainage-imbibition 2D cell was used to relate the optical density to saturation (Colombano et al., 2020; Philippe et al., 2020). The 2D cell used to obtain the correlation curves is made of the same materials (PVDF for the main part, and the same glass at the front of the cell). Measurements were conducted with the same light source and camera. More details on this experimental setup can be found in (Philippe et al., 2020). The results show that a linear relationship between optical density and saturation exists for the oil/ethanol pair ($R^2 = 0.91$). Therefore, it is possible, from the photographs obtained during pumping, to determine the saturation. However, the results are more dispersed for the coal tar/water pair ($R^2 = 0.36$). Due to its opacity, light visualization methods do not apply to complex fluids like coal tars.

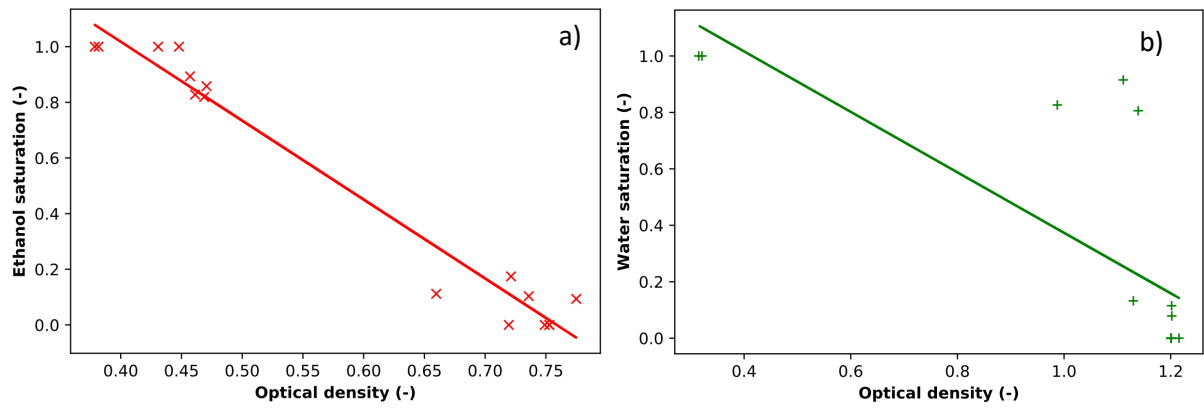
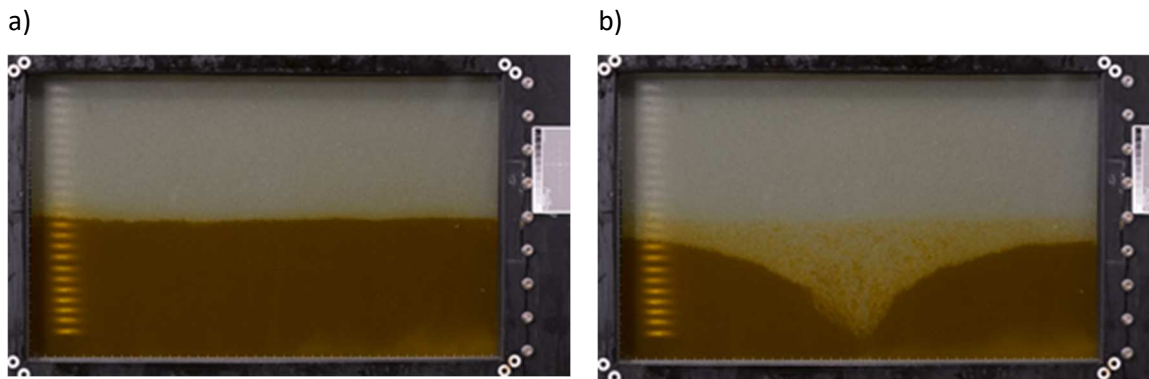


Figure 3 Relationship between optical density and saturation a) ethanol saturation for the oil/ethanol fluid pair, b) water saturation for the coal tar/water pair

For the two fluid pairs, the relationship between optical density and saturation was established at both 20 °C and 50 °C. No effect of temperature on the relationship between optical density-saturation has been observed. Therefore, the same relationships can be used for non-isothermal cases.

To summarize, a pumping experiment can be separated into four stages: a) initial setup of the fluid interface, b) pumping through the central well, c) transformation into shades of gray and determination of the area of interest (AOI), and d) conversion of the light intensity field into a saturation field with the relationship determined above (see Figure 4).



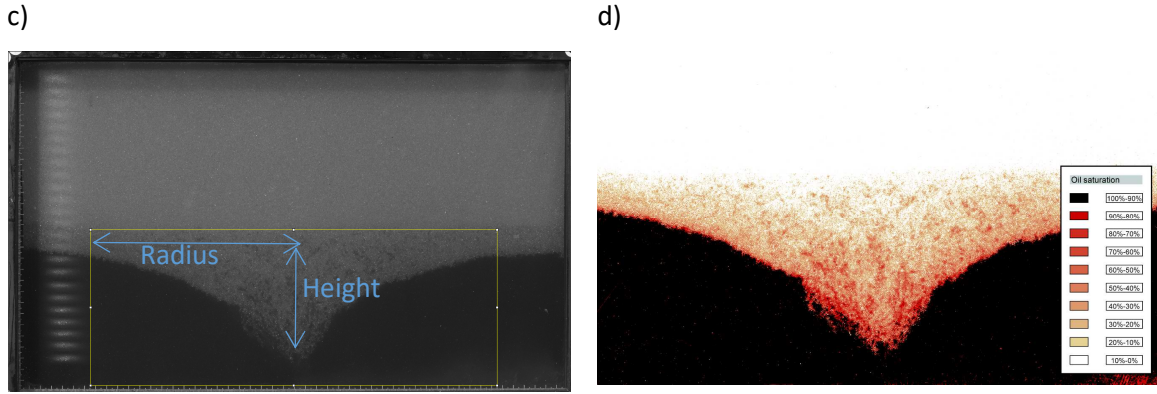


Figure 4 Image interpretation procedure: a) photograph just before pumping; b) photograph after pumping; c) transition to shades of gray and determination of the area of interest (AOI), d) conversion of light intensities into saturation field

3.2. Relative permittivity and saturation calibration

The relative permittivity measurements were carried out on 12 points by TDR sensors. These sensors have recently been used successfully to determine DNAPL saturation in 1D columns filled with glass beads (Iravani et al., 2020; Colombano et al., 2021). These sensors measure relative permittivity values between 1 and 80 (accuracy of ± 1 between 1 and 40). The sensors are placed so that the pins are vertical to reduce their impact on fluid flow. They also measure temperature and electrical conductivity, but these measurements have not been interpreted. The TDR thermocouple sensor is not sensitive enough to measure fast temperature variations, as observed in pumping cases. The use of these sensors to measure temperature was therefore excluded and type K thermocouples were used instead (sensitivity 0.1 s, precision 0.1 °C).

TDR sensors are generally used and calibrated by the manufacturer to measure water content in the unsaturated zone (water/air) from permittivity measurements in static conditions (Davarzani et al., 2014; Gao et al., 2018). Here we were working with another fluid pair as well as in a dynamic regime caused by the pumping conditions. The permittivity measurements should therefore be calibrated on our medium made up of glass beads, and oil/ethanol or coal tar/water to obtain correct saturation values. The Lichteneker-Rother model (Equation 3) has been developed and gives a relationship between relative permittivity and saturation for a three-phase medium made up of two liquid phases and one solid phase (Brovelli and Cassiani, 2008):

$$\varepsilon_r^\alpha = (1 - \varphi)\varepsilon_s^\alpha + \varphi S_w \varepsilon_w^\alpha + \varphi(1 - S_w)\varepsilon_{nw}^\alpha \quad (4)$$

With ε_r the effective relative permittivity measured by the sensor and ε_s , ε_w and ε_{nw} the relative permittivity of the glass beads, wetting liquid (water/ethanol) or non-wetting liquid (coal tar/canola

oil), respectively. $\alpha=0.5$ corresponds to the complex refractive index model (CRIM). For this relationship to work for our pumping experiments, we must use calibration points at known saturation. In addition, at constant saturation, the measured permittivity can be influenced by temperature (Iravani et al., 2020). The temperature measured by thermocouples will be used to correct the permittivity values obtained. Measurements were made at different temperatures for each fluid pair to determine how temperature influenced relative permittivity. During all pumping experiments, the only TDR sensor that can be affected significantly by a change in saturation is K33, located in the bottom row and center of the 2D tank (Figure 2). Figure 5a shows how the two-phase relative permittivity values (i.e., glass beads and a single liquid filling the pore volume) changed as a function of the temperature at this point (between 20 °C and 32 °C) for canola oil and ethanol and Figure 5b shows the same for coal tar and water.

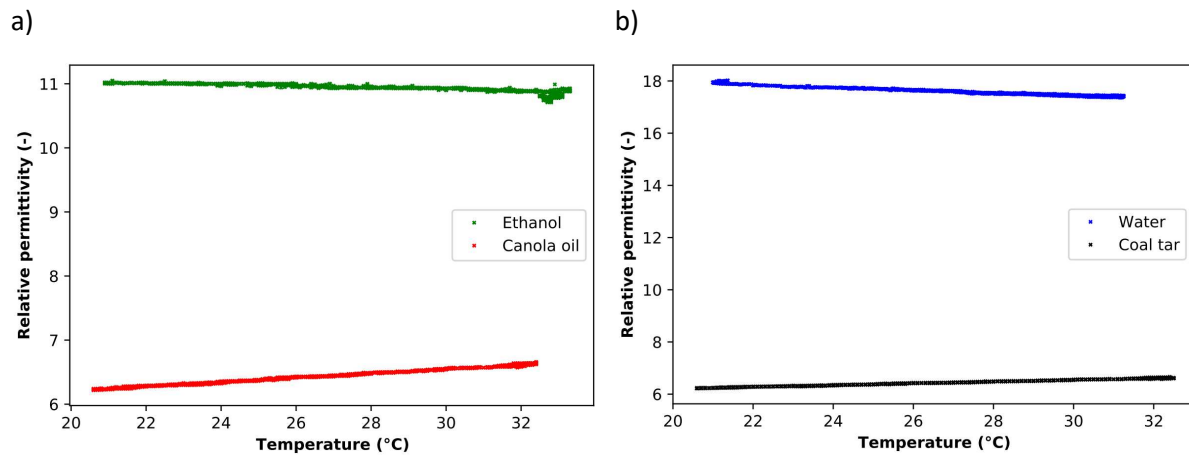


Figure 5 Variations in the relative permittivity as a function of temperature for a) oil and ethanol-saturated glass beads b) coal tar and water-saturated glass beads

In fluid-saturated glass beads, the permittivity of ethanol decreases slightly while that of oil increases with temperature. The same behavior is observed for coal tar and water. This corresponds to the observations of (Iravani et al., 2020). In both cases, we have found linear relationships in the temperature range studied. Therefore, the following relationships can be used to compare permittivity values obtained at different temperatures in glass beads:

Porous media saturated with ethanol $\varepsilon_{r,E}(T) = -1.85 \times 10^{-2} T + 11.4$ (5)
(R²=0.91)

Porous media saturated with canola oil $\varepsilon_{r,O}(T) = -3.45 \times 10^{-2}T + 5.51$ (6)
 (R²=0.92)

Porous media saturated with coal tar $\varepsilon_{r,CT}(T) = -3.26 \times 10^{-2}T + 5.56$ (7)
 (R²=0.91)

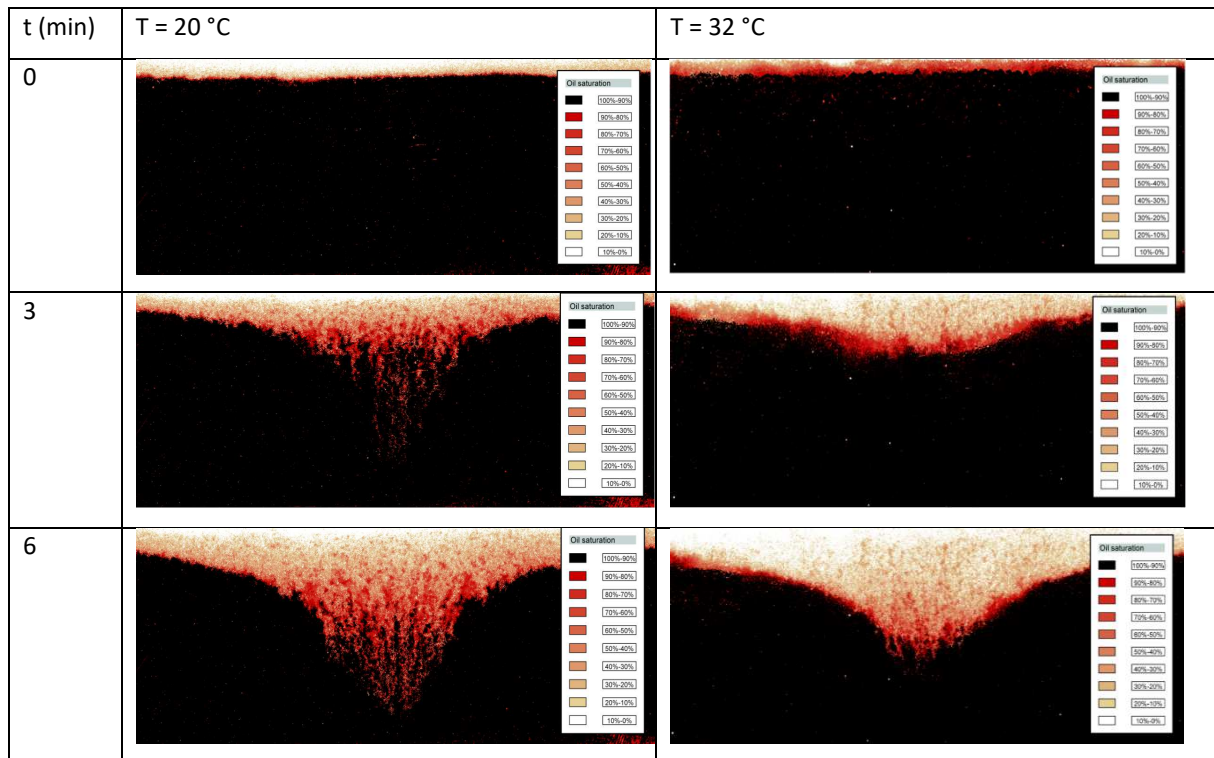
Porous media saturated with water $\varepsilon_{r,W}(T) = -4.99 \times 10^{-2}T + 19.2$ (8)
 (R²=0.97)

4. Results

The results will first be presented for the oil/ethanol pair. This way we see the temperature effect independently of other parameters related to the complexity of coal tar.

4.1. Isothermal two-phase flow

Figure 6 shows photographs converted to oil saturation fields for isothermal pumping experiments at 20 °C and 32 °C.



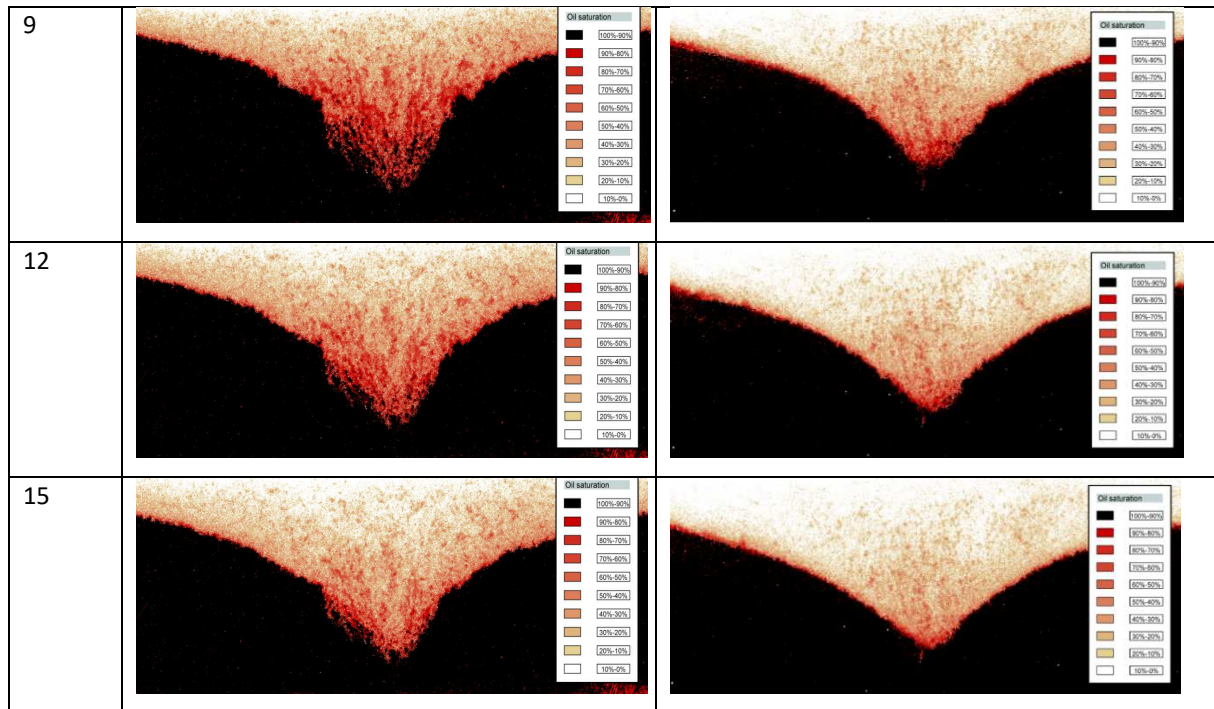


Figure 6 Photographs processed into oil saturation field during pumping at 20 °C and 32 °C, $Q = 100 \text{ mL}\cdot\text{min}^{-1}$.

The oil saturation fields obtained by imaging show distinctively the cone of depression (i.e., the oil/ethanol interface) as well as the presence of residual oil in the form of ganglia throughout pumping.

Ethanol, initially on top of the oil, gradually replaces the oil. The maximum velocity that can be reached inside the tank is equal to the pumping velocity ($2.88 \times 10^{-4} \text{ m}\cdot\text{s}^{-1}$) at all temperatures. For oil/ethanol at 20 °C case, the critical velocity is equal to $U_c = 2.00 \times 10^{-5} \text{ m}\cdot\text{s}^{-1}$, which is lower than the pumping velocity. In this case, viscous fingerings occur around the central area, due to the higher fluid velocity and low viscosity ratio between ethanol and oil ($M = 1.64 \times 10^{-2}$ at 20 °C). We observe less fingering at 32 °C when pre-heating the tank before pumping. At 32 °C, the viscosity ratio and the critical velocity are higher than at 20 °C ($M = 2.18 \times 10^{-2}$; $U_c = 3.31 \times 10^{-5} \text{ m}\cdot\text{s}^{-1}$ at 32 °C). Although the shape of the cone is established around $t = 9 \text{ min}$, it is observed that the oil residual saturation continues to decrease until $t = 15 \text{ min}$ in the cone of depression area.

When comparing saturation fields obtained at 20 °C and 32 °C, it appears that the oil/ethanol interface is smoother during pumping at 32 °C. The pre-heating also reduced the number of viscous fingers forming, thanks to an increase in the viscosity ratio.

4.2. Non-isothermal two-phase flow

4.2.1. Temperature profiles

Pumping in isothermal conditions has demonstrated the advantages of heating the tank and the viscous DNAPL before pumping. Non-isothermal conditions, which simulate local heating, are closer to

situations encountered on real sites. Temperature variations measured at the thermocouples are shown in Figure 7 during the entire 100 mL.min⁻¹ pumping experiment (heating and pumping steps). The initial time (t=0) represents the start of the heating step. In Figure 8, temperatures are shown only during pumping for the experiment at 100 mL.min⁻¹ with t = 0 representing the start of the pumping step. The temperature on the left (T11 and T31) of the 2D tank, near the heating element, increased quickly and reached a steady temperature of 48 °C. The increase in temperature caused by heating is also visible on the second column of thermocouples (T12, T32, and T22), reaching between 27 °C and 35 °C. The temperature of the rest of the tank is between 20 °C and 25 °C and does not seem to be affected by the heating element. Variations in the outside temperature should also be noted and are notably responsible for the general decrease in values after 15 hours of heating.

During pumping, temperatures ultimately had small variations, except on the thermocouples located near the center (T22 and T23). The temperature rises from 25 °C to almost 30 °C, due to the replacement of oil by ethanol at higher temperatures.

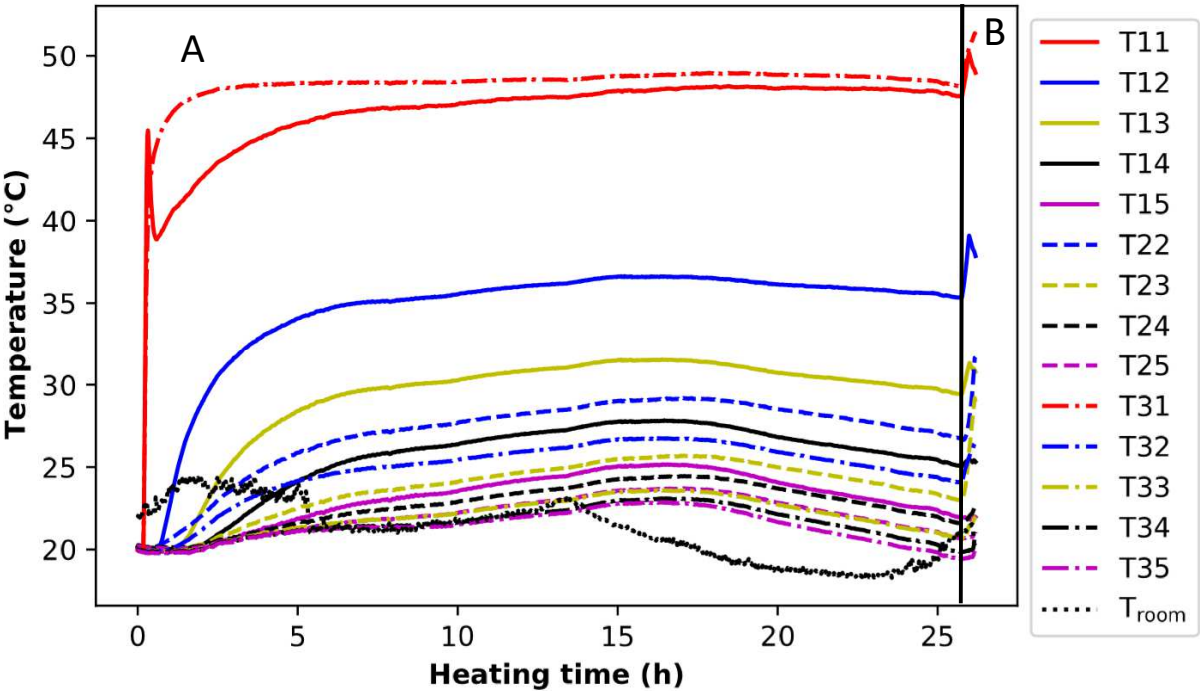


Figure 7 How temperature changed during the experiment (A: heating and B: pumping) under non-isothermal conditions (Q= 100 mL.min⁻¹); t = 0 represents the start of the heating and the vertical black line is the start of the pumping

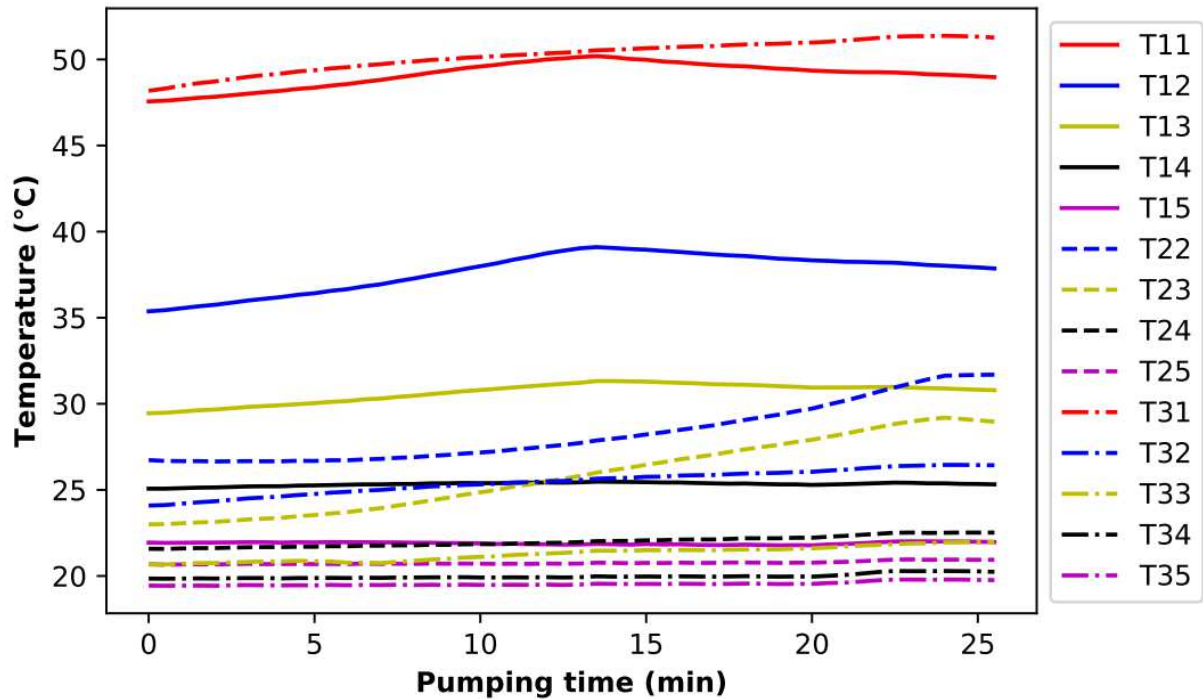


Figure 8 How temperature measured with thermocouples only changed during pumping ($Q = 100 \text{ mL}\cdot\text{min}^{-1}$); $t = 0$ presents the start of pumping

4.2.2. Saturation fields

Figure 9 shows the oil saturation fields during pumping under non-isothermal conditions at pumping flow rate of $Q=100 \text{ mL}\cdot\text{min}^{-1}$ compared to the $20 \text{ }^\circ\text{C}$ isothermal case at the same flow rate.

Some observations join those already carried out on isothermal cases: viscous fingerings appear during pumping in the central part of the tank (significant between $t = 3 \text{ min}$ and $t = 9 \text{ min}$) until a smoother cone of depression is visible at the end of pumping ($t = 15 \text{ min}$). In addition, it also seems that the cone is slightly unsymmetrical at $t = 3 \text{ min}$, with a greater cone height on the left (compared to the central pumping point) than on the right. Also, we can see that the residual saturation is higher in the right of the tank than the left. This is linked to the temperature field gradient during the heating step. This heating gradient causes the properties of canola oil and ethanol to change due. The critical velocity varies between $2.00 \times 10^{-5} \text{ m}\cdot\text{s}^{-1}$ at $20 \text{ }^\circ\text{C}$ and 3.31×10^{-5} at $32 \text{ }^\circ\text{C}$ inside 2D tank. The viscosity ratio also increases from 1.64×10^{-2} at $20 \text{ }^\circ\text{C}$ to 2.64×10^{-2} at $32 \text{ }^\circ\text{C}$. Thus, the critical velocity and the viscosity ratio are higher in the left of the tank than the right, creating a difference in fingering number in the tank. In the end, residual saturation is also variable inside the tank depending on the temperature.

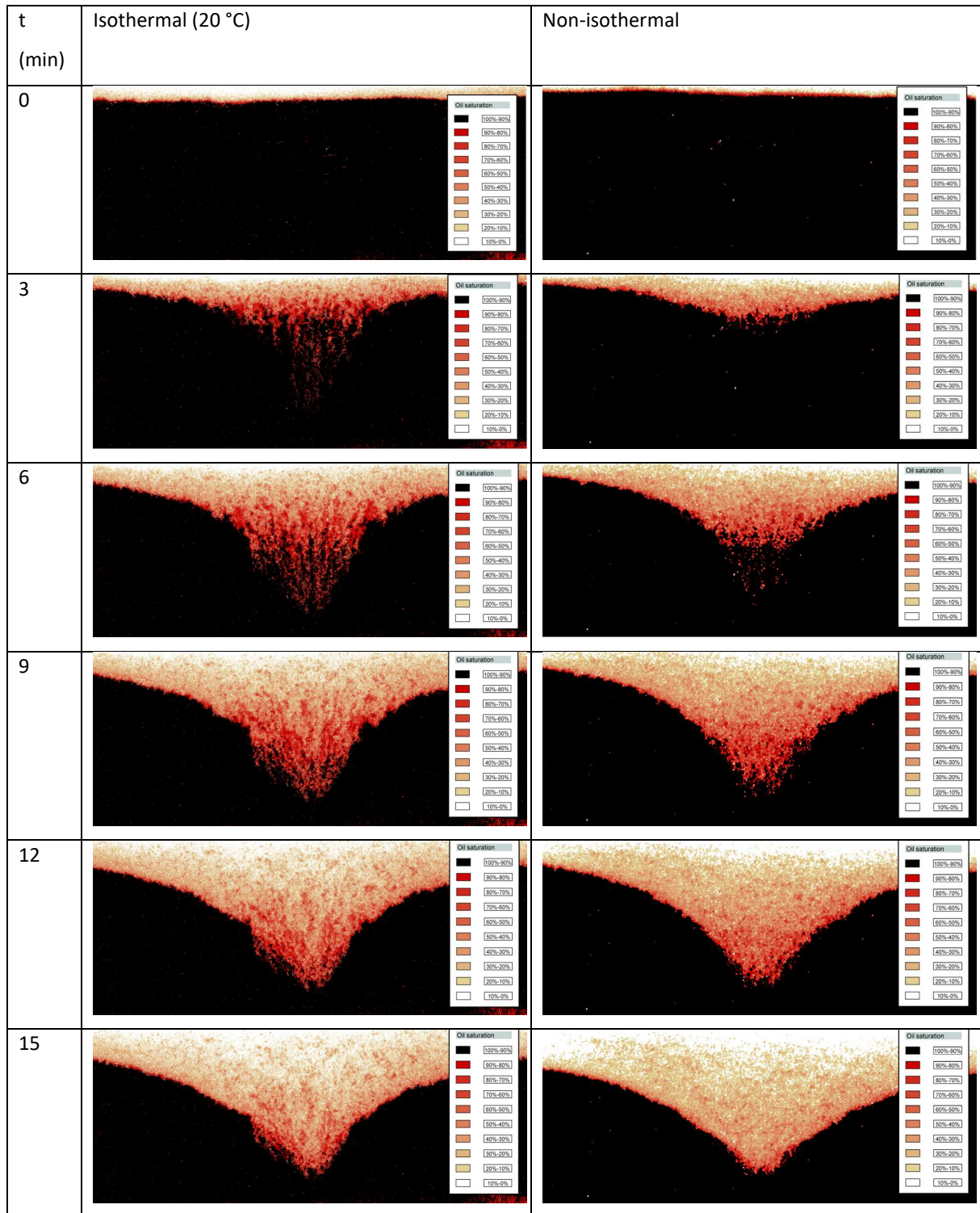


Figure 9 Photographs taken and processed into oil saturation fields during pumping in non-isothermal conditions and their comparison to isothermal 20 °C case at $Q = 100 \text{ mL}\cdot\text{min}^{-1}$

4.3. Effect of flow rate on non-isothermal two-phase flow

The presence of viscous fingers was still observed at $100 \text{ mL}\cdot\text{min}^{-1}$ in non-isothermal conditions. The pumping velocity is still higher than the critical velocity at which the flow is unstable. A pumping

experiment at $20 \text{ mL}\cdot\text{min}^{-1}$ was done to observe the cone of depression and the saturation field in stable flow conditions.

The effect of the pumping flow rate on the temperature distribution in the tank is shown in Figure 10. Temperature fields obtained with Surfer (using the kriging method) are also presented in Appendix A (Figure A. 2). For both flow rates investigated here ($20 \text{ mL}\cdot\text{min}^{-1}$ and $100 \text{ mL}\cdot\text{min}^{-1}$), the temperature increases during pumping on T12, T22, T33. However, this increase is greater for the higher flow rate ($100 \text{ mL}\cdot\text{min}^{-1}$). A higher pumping rate effectively increases thermal advection in the tank. Therefore, the generated heat from the heating element is better transferred to the rest of the tank. The calculation of the Rayleigh number Ra (see Appendix A, Table (A. 1)) showed that the natural convection should be considered in the wetting-phase zone.

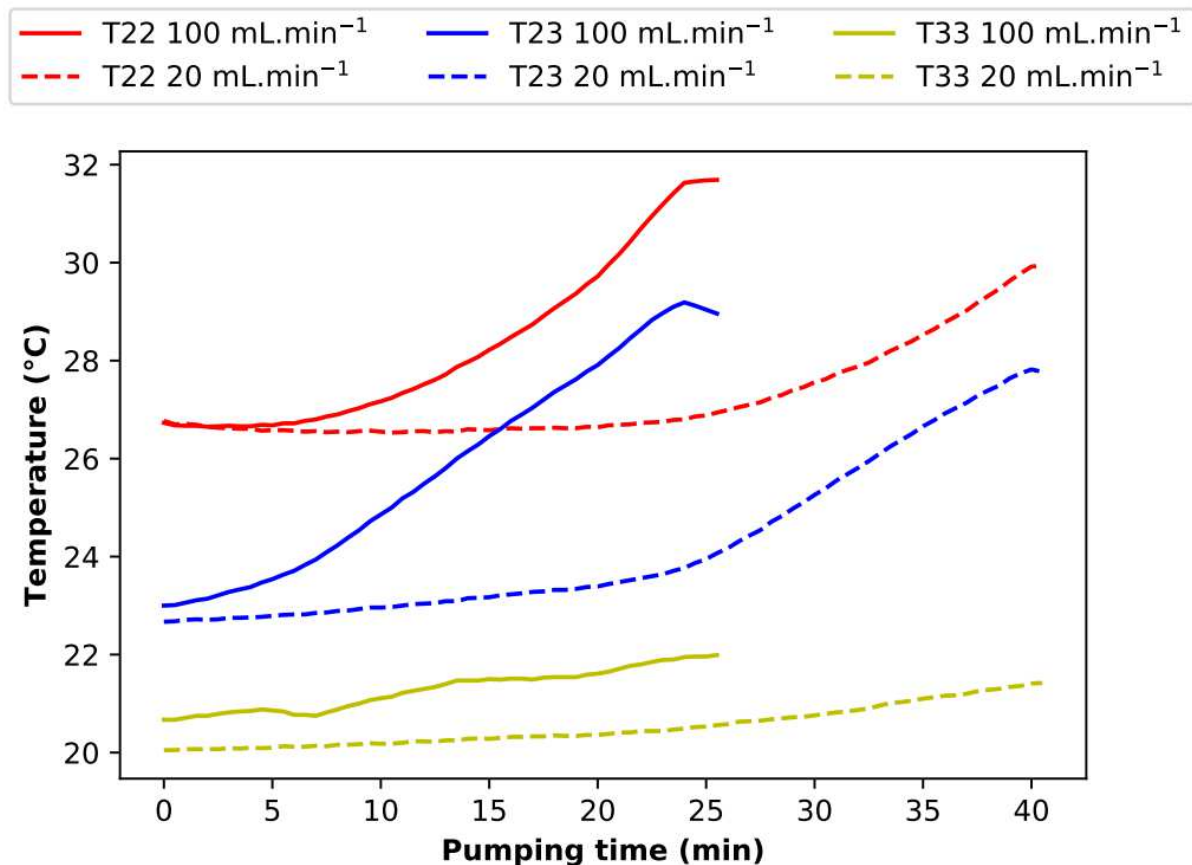
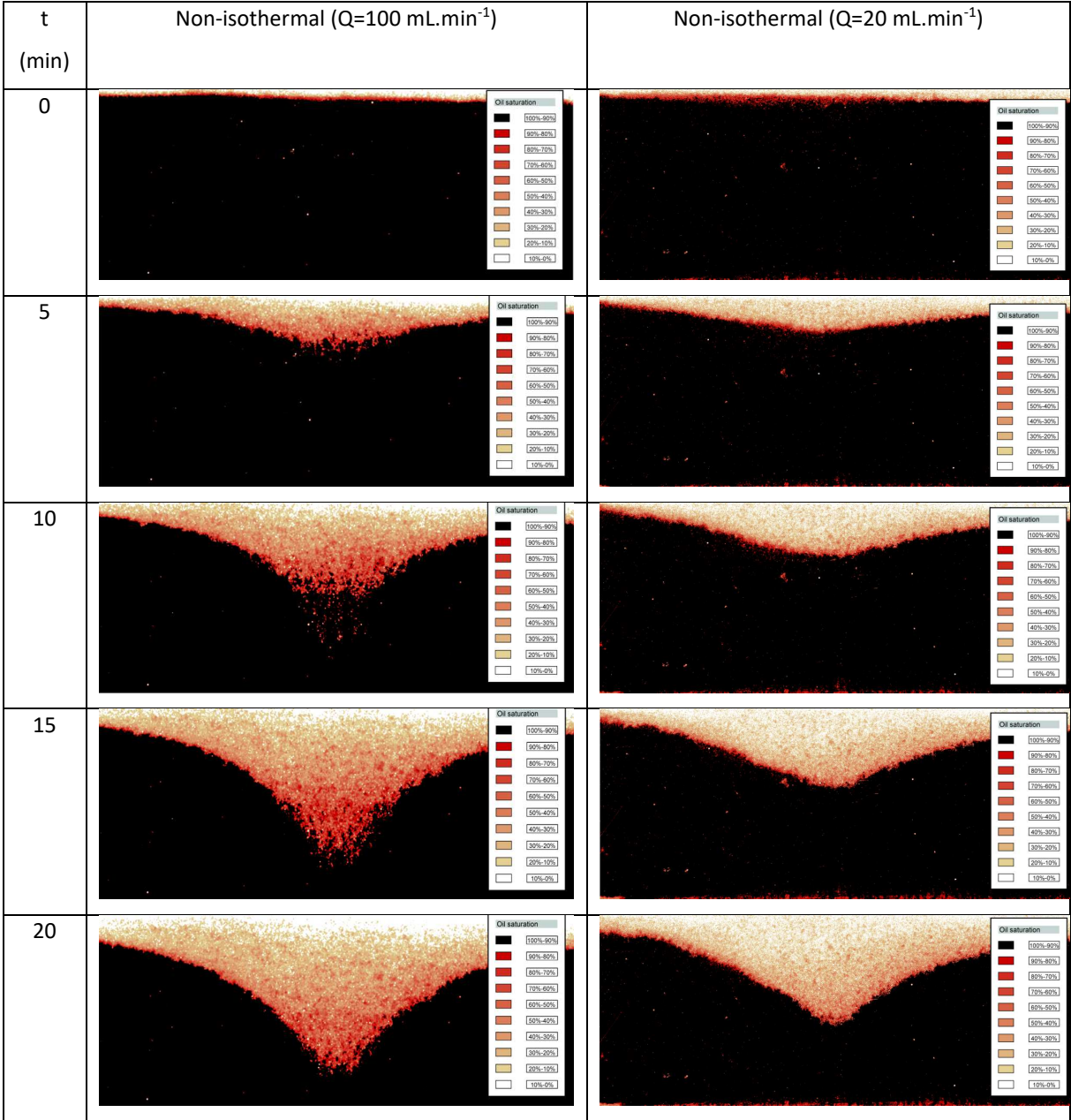


Figure 10 Effect of the pumping rate on the temperature change during pumping

The comparison between saturation fields obtained for both flow rates is presented Figure 11. Regarding the pre- and post-treatment photographs obtained at $20 \text{ mL}\cdot\text{min}^{-1}$, no viscous fingering has been observed throughout the pumping. In this case, the pumping velocity is equal to $5.76 \times 10^{-5} \text{ m}\cdot\text{s}^{-1}$, much closer to the order of magnitude of the critical velocity ($10^{-5} \text{ m}\cdot\text{s}^{-1}$). Thus, the absence of viscous

fingering at 20 mL.min⁻¹ can be explained by a much more stable interface than at 100 mL.min⁻¹. Also, the time needed to reach the steady-state is longer (40 min) and the saturation in the residual zone is much smaller than we observed at 100 mL.min⁻¹. The interface is smoother throughout pumping and better describes a cone of depression typically represented using multiphase Darcy's laws. However, from t = 25 min, we notice many oil “ganglia” present in the residual zone. This number of ganglia is much higher on the right of the cone of depression, less influenced by the heating than the left. The number and size of these ganglia are bigger for higher flow rate.



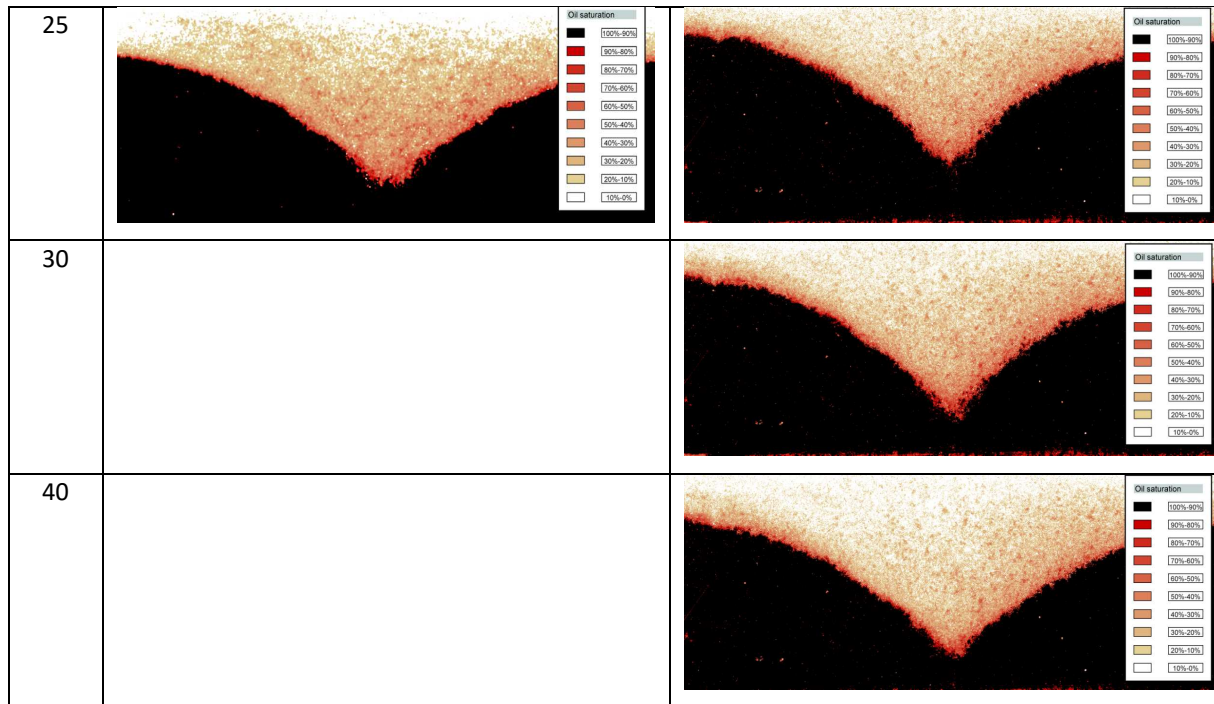


Figure 11 Comparison of the oil saturation fields after pumping in non-isothermal conditions for two pumping rates (20 mL.min⁻¹ and 100 mL.min⁻¹)

5. Discussion

5.1. Evaluation of saturation and residual saturation

The change in ethanol saturation near the pumping point (TDR K33) is shown in Figure 12 as a dotted line for different pumping cases. The calculated averaged saturations around the TDR K33 (radius 1 cm), obtained by imaging, are also presented in the form of a point on this same graph. We should note that the LRM gives a pixel-scale saturation field and TDR gives centimeter-scale saturation. The corresponding imaging technique saturation, reported in Figure 12, comes from averaging the pixel-scale saturation over a surface to obtain a centimeter-scale quantity. Later we will validate the imaging technique against the mass recovery.

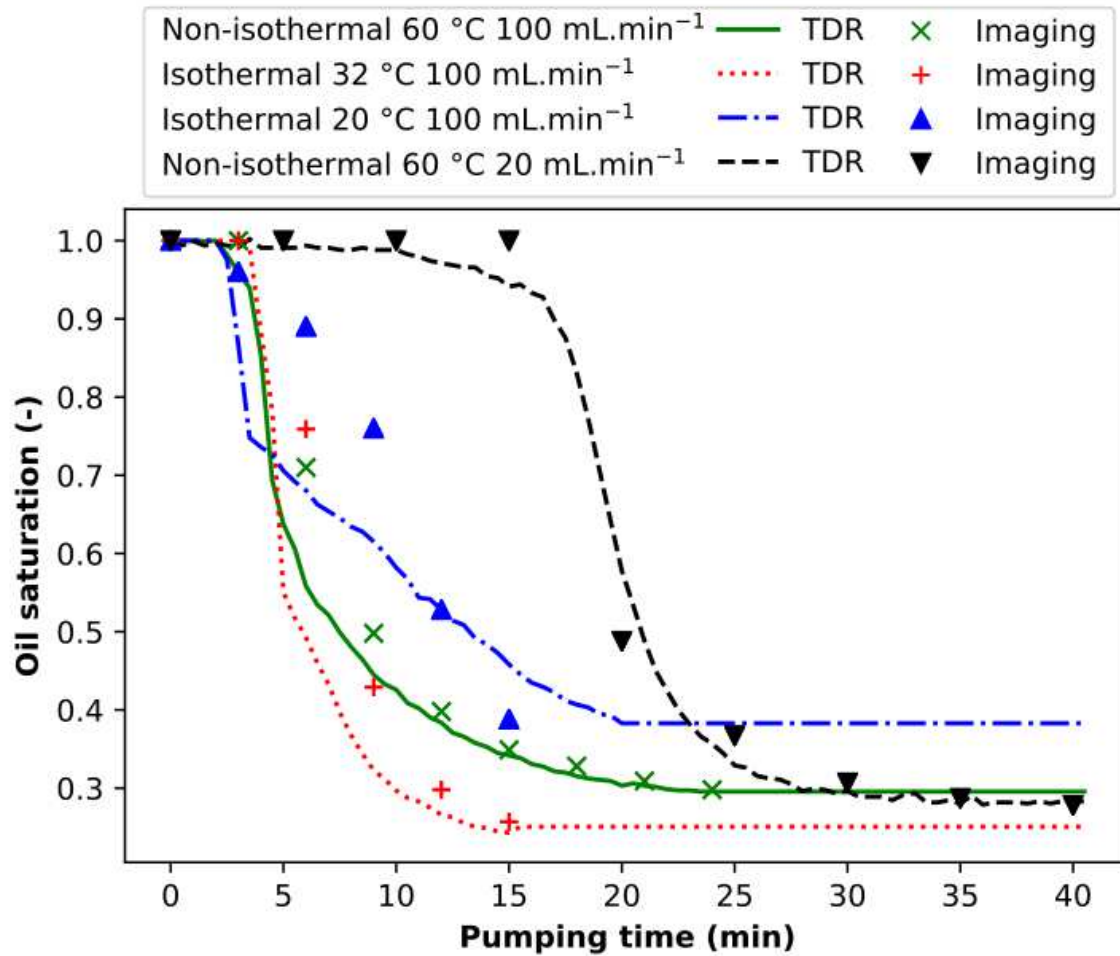


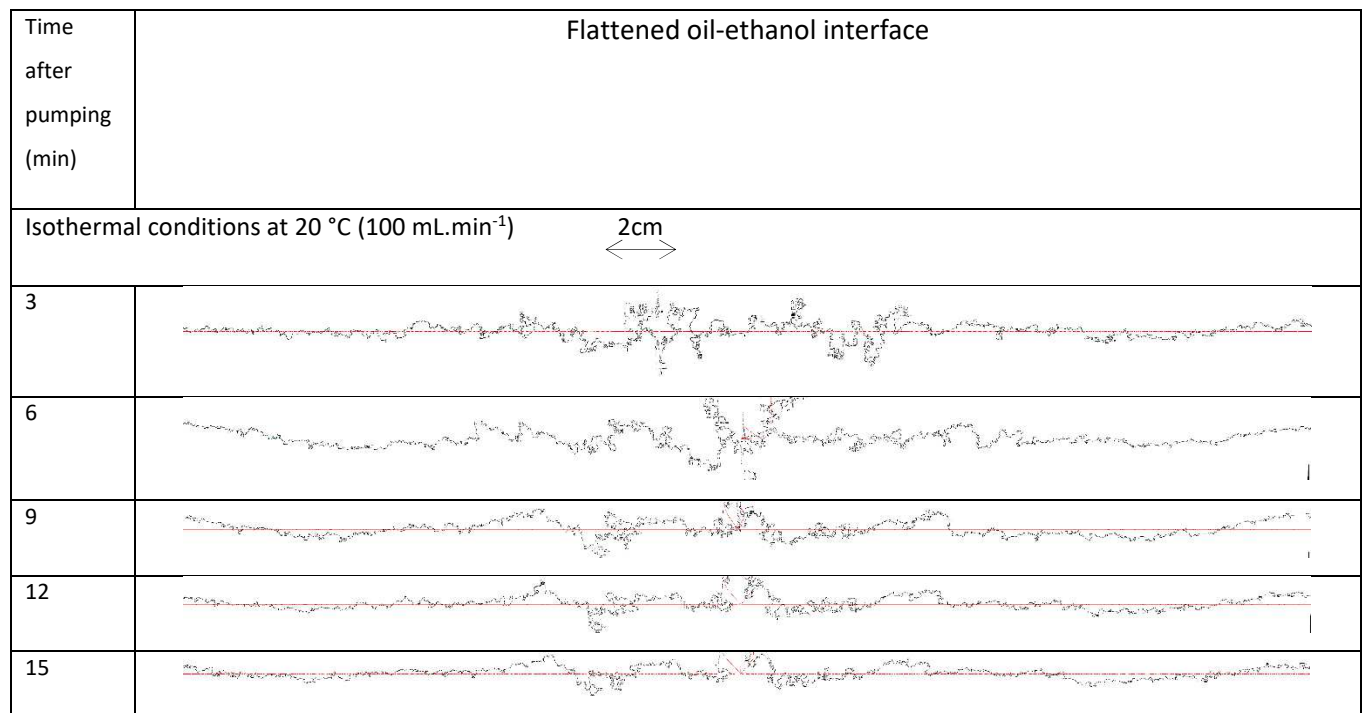
Figure 12 Effect of temperature and flow rate on changes in ethanol saturation (K33) near the pumping point in the 2D tank. The profiles are extended up to $t = 40$ min to compare the residual saturations. The points correspond to the saturation on K33 calculated by imaging.

In non-isothermal conditions, the residual saturation is lower (0.28) than that observed at the isothermal 20 °C case (0.40). Moreover, reducing the flow rate does not seem to significantly decrease residual oil saturation in this zone. Finally, the time required for the ethanol to be detected at the TDR sensor increases when pumping is performed at higher temperature. Ethanol replaces the oil initially present in a smaller pore volume because of the greater number of viscous fingers at low temperature. In this case, the flushing fluid (ethanol) will therefore reach the pumping point in a shorter time and leaves a higher volume of trapped oil in the tank. This observation is confirmed from the images taken during pumping: the number of fingers decreases during the experiments with heating or at high temperature, and the height of the cone is the greatest at 20 °C. In addition, the lowest residual saturation (0.25) is still obtained in the isothermal case at 32 °C. It is interesting to note that even though the fluid interface front passed the sensor level, oil saturation keeps on decreasing afterward. The rate of decrease depends on the presence and the amount of the fingering. This can be explained

by the dynamic effect and remobilization of the discontinuous non-wetting phase ganglia by the flow of wetting phase towards the pumping well. Also, we see that the saturation values estimated by imaging and TDR are quite close, except for the experiment at 20 °C under isothermal conditions. The presence of more fingers and ganglia in the 20 °C isothermal experiment is a possible explanation for these differences. Therefore, it should be possible to use TDR measurements to evaluate coal tar saturation during coal tar/water experiments.

5.2. Fingering evaluation

The fingers were measured as the difference between the interpolated profile corresponding to the oil/ethanol interface and the actual profile on all the pixels. The method that we used to determine the interface is different from the saturation conversions and does not require such a high range of optical densities. The photographs were converted to binary images (0 for coal tar, 1 for water) with thresholding. The same threshold value and method was applied for all coal tar/water photographs. The processes were executed with Fiji (ImageJ). With this method, we can distinguish the main line separating both liquids, referred as the interface. The obtained interface results using ImageJ fit the DNAPL/water interface observation. This method does not allow us to distinguish between viscous and capillary fingering. The flattened fingers using Fiji at the oil/ethanol interface during pumping at 20 °C and 32 °C, and in non-isothermal conditions are shown in Figure 13. The scale is the same on each fingering profile.



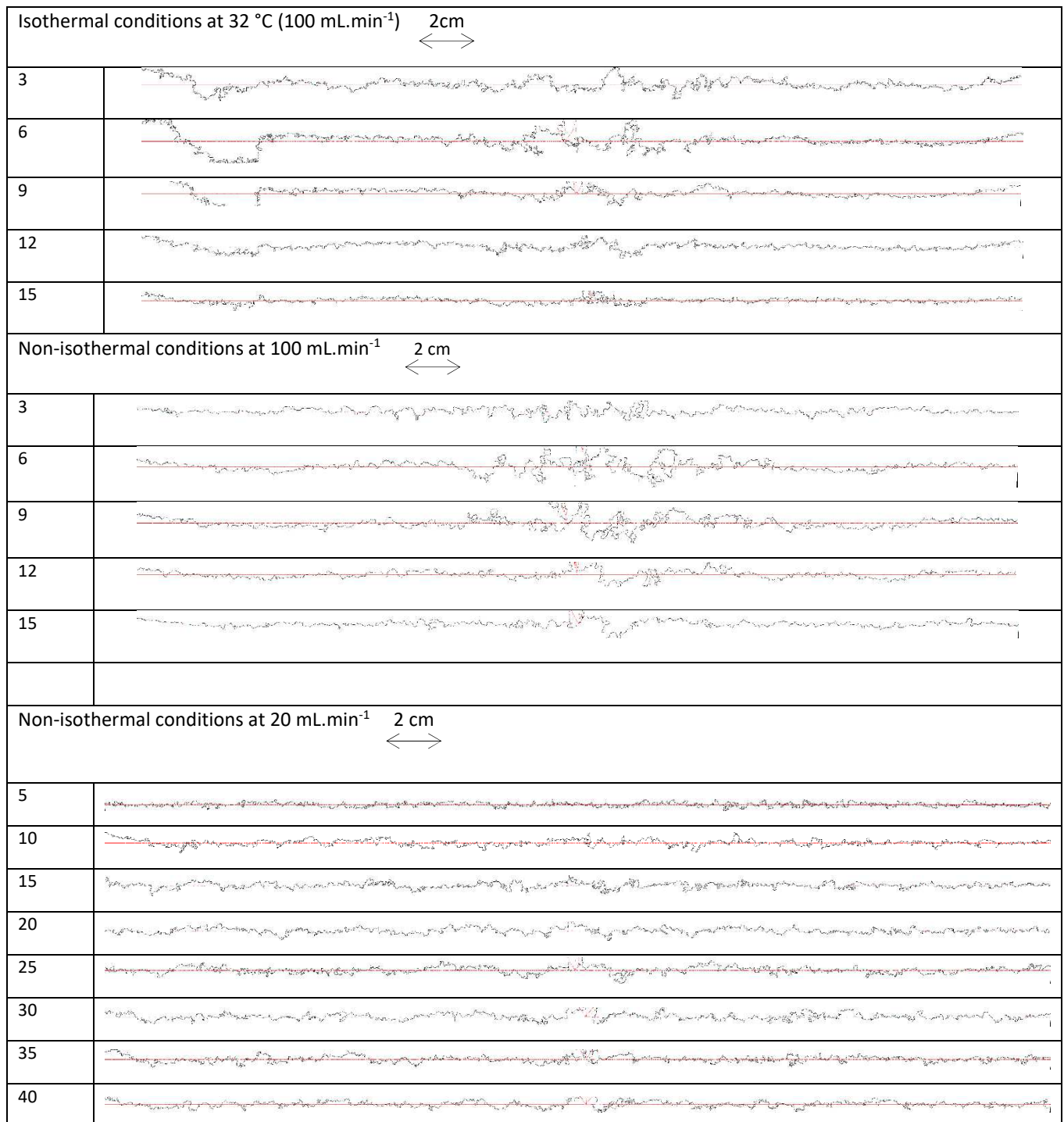


Figure 13 How fingering changes at the oil/ethanol interface during oil pumping under isothermal conditions at 20 °C and 32 °C, and non-isothermal conditions ($Q=100 \text{ mL}\cdot\text{min}^{-1}$)

The size of the fingers initially increases as the cone of depression is formed. This trend is consistent with observing the formation of viscous fingerings during pumping at the interface on experiments at $100 \text{ mL}\cdot\text{min}^{-1}$. Also, higher fingers are formed near the center of the tank than on the left and right sides. Then the fingering effects decrease once the ethanol begins to be recovered until it reaches an interface with a few fingers, especially visible in the non-isothermal case, and the case at 32 °C. Heating the tank reduces the length of the fingers at any time. The main differences are mostly towards the

center, near the pumping point. This result is consistent with the fact that the oil/ethanol viscosity ratio is lower at 32 °C than that at 20 °C. In the non-isothermal case, the fingers are shorter than those observed at 20 °C but still longer than for the case at 32 °C. The fingering patterns at 20 mL.min⁻¹ also do not have large fingers at the center. A lower number of fingers indicates that more oil is recovered since it is not trapped during pumping. Thus, pumping at low flow rate effectively increases the oil volume extracted from the tank, but the pumping time is also increased accordingly.

The average size of the fingers is also calculated between pumping in non-isothermal and isothermal conditions at 20 °C, separately in the left and right parts of the tank. The point separating these two parts is chosen as being the lowest point of the cone of depression determined from image analysis.

Table 5 summarizes the mean and maximum observed finger length for the pumping experiments in isothermal (20 °C) and non-isothermal conditions at 100 mL.min⁻¹.

Table 5 Comparison of how fingerings change at the oil/ethanol interface during oil pumping under non-isothermal conditions (Q= 100 mL.min⁻¹)

Experiment (100 mL.min ⁻¹)	Side	Average length (cm)	Maximum length (cm)
Isothermal 20 °C	Left	0.20	0.84
	Right	0.21	0.81
Non-isothermal 60 °C	Left	0.08	0.33
	Right	0.17	0.77

In the case of pumping at 20 °C, the mean and maximum finger sizes are basically of the same order of magnitude in the left and right sides of the tank (0.20 cm and 0.80 cm). In the non-isothermal case, however, the fingers in the left of the tank are much smaller (0.08 cm and 0.33 cm) than the right (0.17 cm and 0.77 cm). The length of the fingers is therefore reduced when pumping in a pre-heated tank (non-isothermal conditions) rather than at isothermal 20 °C.

5.3. Recovery efficiency

The recovered oil volumes, estimated by imaging from analyzing the cone of depression zone, are shown in Figure 14. Comparison of this data with mass scale measurements are also shown. We found great agreement between oil volume measured with mass scale and estimated by imaging data for all experiments before breakthrough. However, we noted that the mass measurements are a little overestimated compared to the quantity of oil recovered estimated by imaging. This is because a small part of ethanol bubbles and oil/ethanol emulsion started to be recovered near the breakthrough point and is included in the mass measurements. We could not separate both liquids directly during the

experiments and this results in a slight overestimation of the oil volume recovered compared to the oil volume estimated with imaging on the figure.

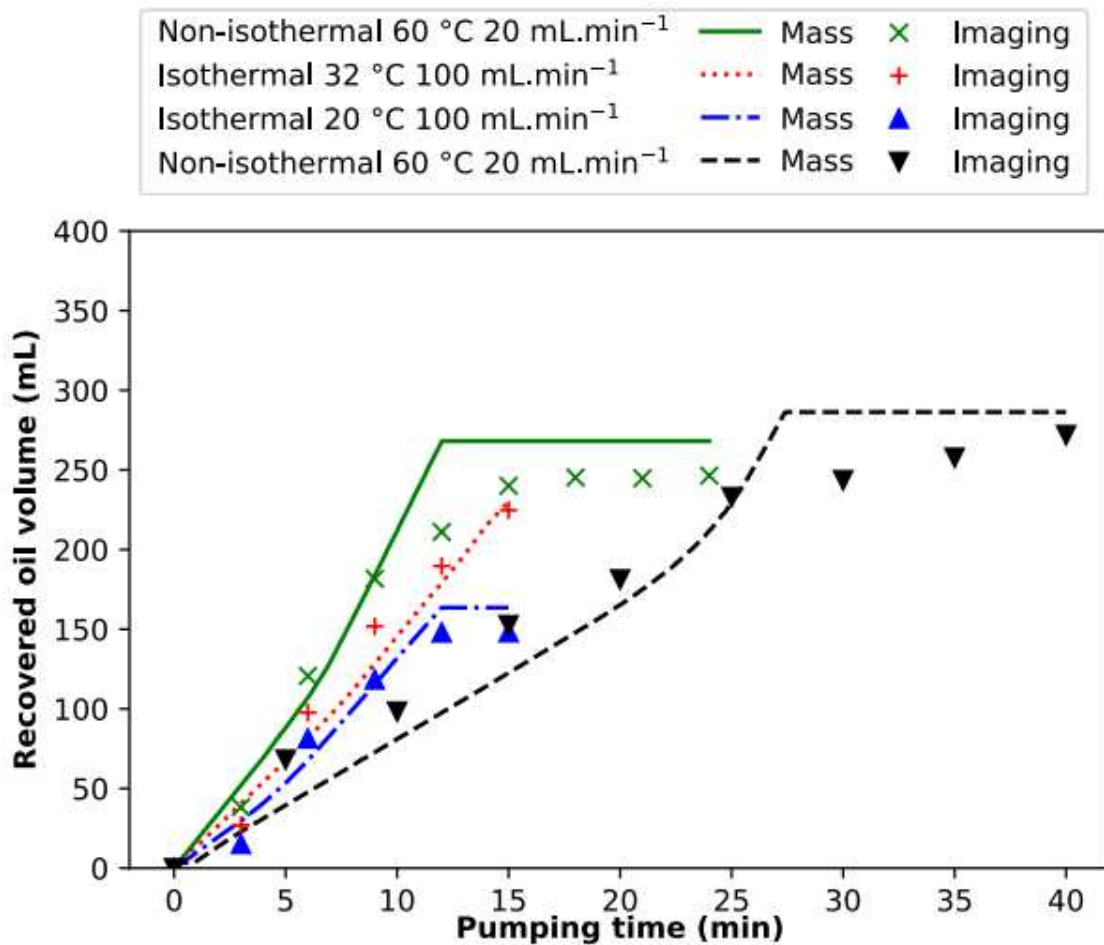


Figure 14 Volume of oil recovered (estimated by imaging as markers and measured with mass scale as lines) as a function of pumping time

Isothermal pumping at 32 °C recovers more oil than at 20 °C. Pumping under non-isothermal conditions recovers more oil than isothermal pumping. A lower flow rate (20 mL.min⁻¹) collects a higher volume of oil from the tank than at a high flow rate (100 mL.min⁻¹).

Table 6 shows the radius of influence, the residual saturations in the cone at the end of pumping and for the left and right of the cone of depression zone, and the remediation efficiency values, obtained by imaging, for each oil pumping experiment.

Table 6 Summary of variables at the end of the pumping

Experiment	Radius of influence (cm)	Estimated residual saturation in the depression cone			Remediation efficiency (%)
		Left	Right	Total	
Isothermal 20 °C 100 mL.min ⁻¹	14.89	0.36	0.37	0.36	70.53
Isothermal 32 °C 100 mL.min ⁻¹	15.40	0.20	0.21	0.20	81.15
Non isothermal 60 °C 100 mL.min ⁻¹	14.84	0.28	0.31	0.30	76.96
Non isothermal 60 °C 20 mL.min ⁻¹	15.12	0.20	0.27	0.24	81.85

We found that an increase of only 12 °C reduces the residual saturation from 0.36 to 0.20. Moreover, we observed improved remediation efficiency linked to a slight increase in the radius of influence and a decrease in viscous fingerings. Heating the left side of the tank to 60 °C before pumping at 100 mL.min⁻¹ (non-isothermal conditions) also reduced the residual saturation and increased the efficiency compared to pumping at 20 °C. However, pumping at 32 °C was still more efficient than pumping under non-isothermal conditions. In addition, in non-isothermal conditions, the lower pumping rate slightly increased the radius of influence as well as the efficiency. The residual saturation also decreased, thanks to a reduction in the formation of viscous fingers during pumping. The residual saturation estimated by imaging in the cone of depression was almost identical between the left and right parts of the pumping in isothermal cases, while it was lower by 3% at 100 mL.min⁻¹ and 7% at 20 mL.min⁻¹ in non-isothermal conditions. Finally, the residual saturations estimated by imaging are still close to the ones directly measured with the TDRs. For instance, at 20 °C, the measured residual saturation is 0.40 while it is equal to 0.36 when considering the whole residual zone of the tank.

The masses measured using the automatic balance were converted to mass flow rates (by interpolation) in Figure 15 for oil/ethanol. Initially, pumping only recovers oil (constant flow) until the breakthrough time, which is different for each experiment. This breakthrough time represents the point at which ethanol begins to be recovered as well.

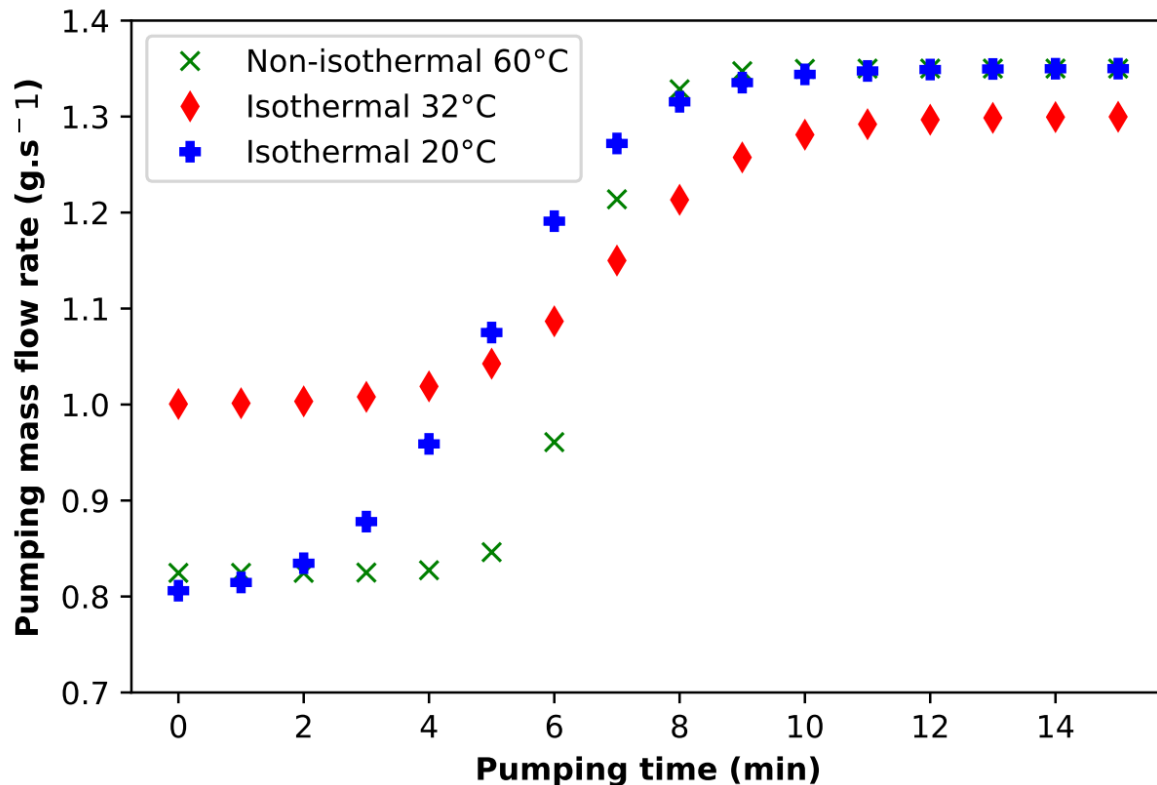


Figure 15 Recovery rate observed for central pumping at the same pump rotation speed (84.3 rpm: 100 mL.min⁻¹ for ethanol) under isothermal (20 °C, 32 °C) and non-isothermal (side heating at 60 °C) conditions

After this breakthrough time, the oil is no longer pumped, and a new constant value is reached where only the ethanol is recovered: the residual saturation is reached. The breakthrough time increases when the tank is heated. This is due to the reduction of viscous fingers in the tank, which allows the oil to be pumped for a longer time, and therefore increases the remediation efficiency. The initial and final flow rates between the 20 °C isothermal case and the non-isothermal case are equal. However, the ethanol arrived later, and the oil/ethanol mixture is recovered for a shorter time. The temperature at the pumping point is effectively 20 °C but the lower viscosity ratio allows oil to be recovered for a longer time.

6. Real DNAPL/water case

Experiments with oil/ethanol have provided a better understanding of how heating can affect the recovery of a viscous dense liquid phase in a saturated medium. A temperature increase is linked to a residual saturation decrease and an increase in the pumping radius.

The coal tar used here has, in fact, more variable properties because of its chemical complexity. Also, the coal tar adheres to the glass internal wall of the tank and is opaque to visible light, so the previous imaging techniques cannot be used to estimate the water saturation. Even if the water-coal tar

interface can be distinguished, the saturation calculations are generally wrong because coal tar completely absorbs visible light. In this case, the optical density measurements do not have a range sufficient to convert them into saturation. When we converted the photographs into grayscale images, we observed shades of gray corresponding to different saturations for oil/ethanol. However, that was not the case for coal tar/water.

The initial tank preparation and the heating phase did not present any problems. However, during the pumping phase, the measured flow rate was much lower when recovering the coal tar. Instead of the 15 minutes used for the oil, the pumping took 45 minutes before reaching a steady state. The sticky nature of the coal tar and clogging effects in the tubing could both explain this difference. Grayscale images taken during coal tar pumping are shown in Figure 16.



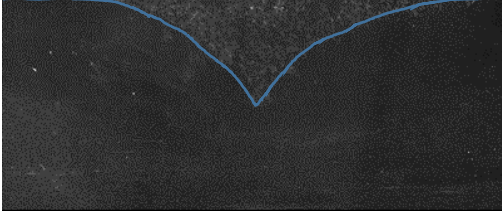
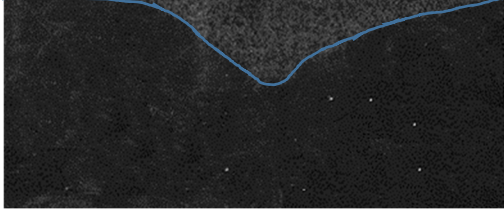
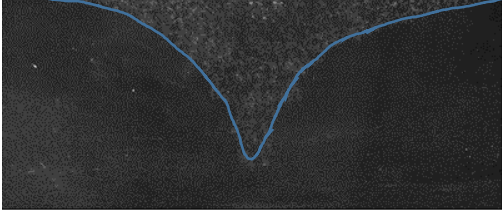
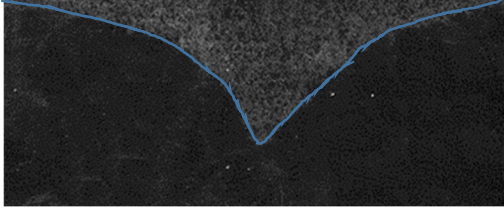
t (min)	T = 20 °C	t (min)	Non-isothermal
0		0	
15		20	
30		45	

Figure 16 Comparison of the grayscale images after coal tar pumping in isothermal conditions 20 °C and non-isothermal conditions for $Q=100 \text{ mL}\cdot\text{min}^{-1}$

6.1. Temperature and saturation results

The thermal properties of the oil/ethanol and coal tar/water fluid pairs are quite different. The thermal conductivity and specific heat capacity of the oil used is indeed quite close to that of coal tar, but ethanol's is much lower than water's. The temperature profiles measured at the thermocouples are presented in Figure 17. The temperature increases significantly when pumping on T11, T12, T22, T23, T31. These increments correspond to the arrival of heated water during pumping. Temperature fields obtained with Surfer are also presented in Appendix A, Figure A. 3.

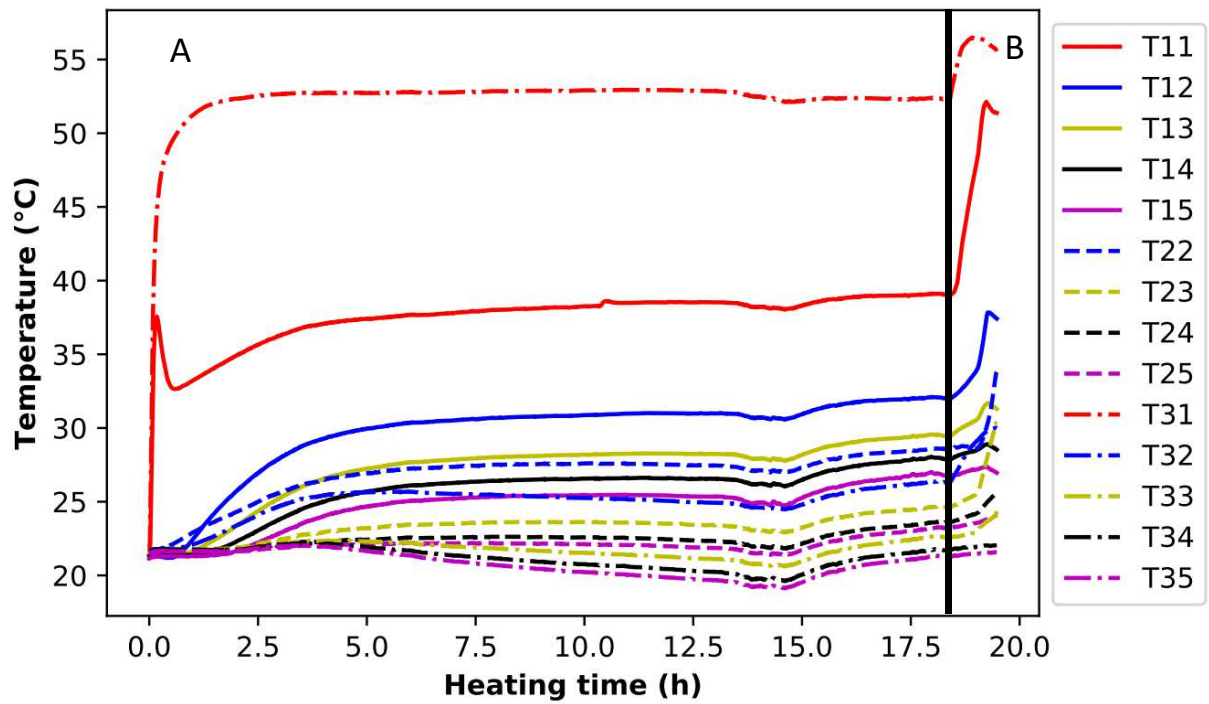


Figure 17 Thermocouple temperature profiles during the coal tar/water fluid pair experiment (A: heating and B: pumping) under non-isothermal conditions. $t = 0$ represents the start of the heating and the vertical bar the start of the pumping

The saturation profiles have been plotted using TDR data. Figure 18 compares the coal tar saturation measured at the sensor (K33) in isothermal conditions (20 °C) and non-isothermal conditions (heating setpoint 60 °C).

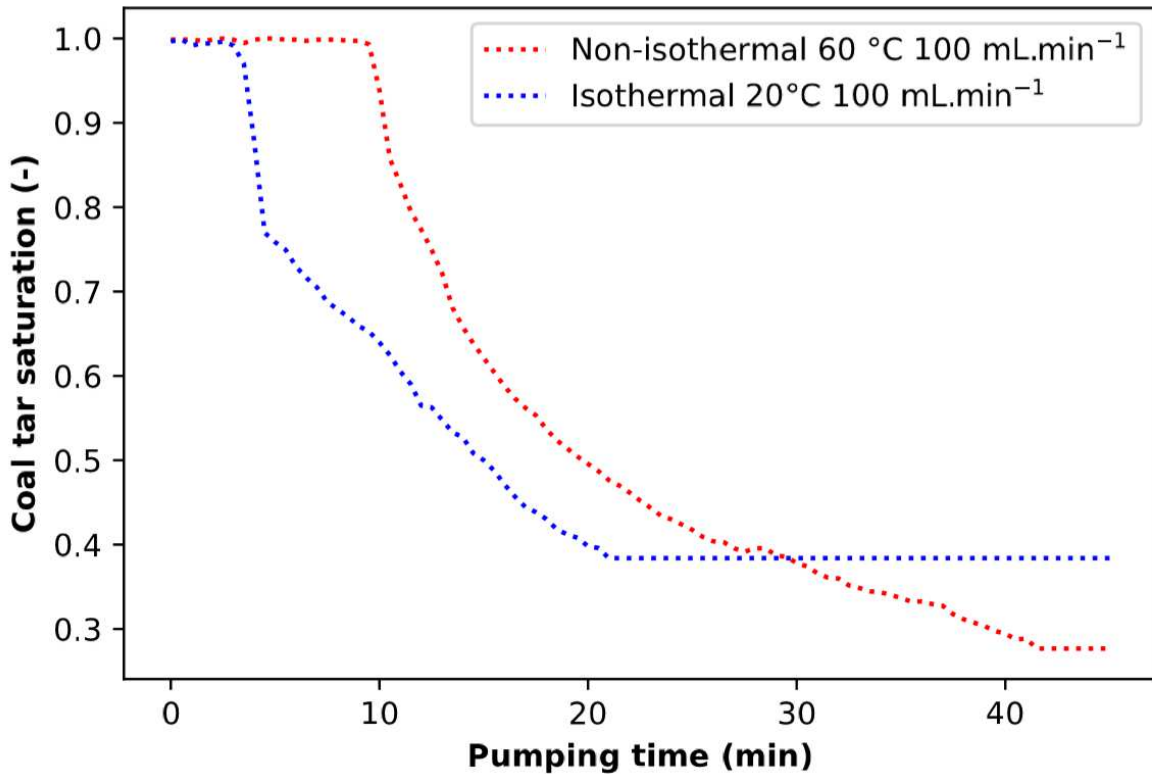


Figure 18 How saturation changed (K33) for pumping coal tar in non-isothermal conditions and isothermal conditions (20 °C) at Q=100 mL.min⁻¹

Coal tar residual saturation was estimated to be 0.39 at 20 °C. Pre-heating at 60 °C the left side of the tank before pumping coal tar reduces this value to 0.27. The reduction is similar to that observed for oil/ethanol (from 0.40 at 20 °C to 0.28 in non-isothermal conditions).

6.2. Fingerings

Even if the estimation of coal tar saturation is not accurate using imaging, it is still possible to interpolate the coal tar/water interface with binary images (0 = coal tar, 1 = water) and thresholding. Thus, we can still measure the fingers in the case of coal tar. Figure 19 shows how the fingers changed during pumping.

Time after pumping (min)	Flattened coal tar-water interface
	Non-isothermal conditions at 100 mL.min ⁻¹ 2 cm ↔
10	
20	

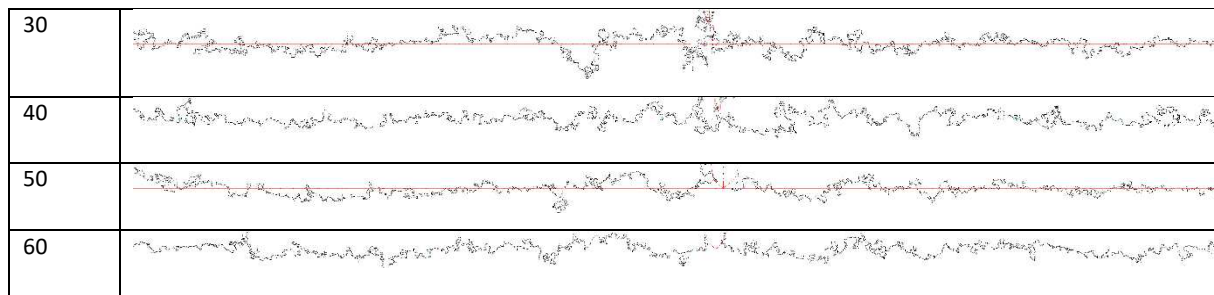


Figure 19 How fingering at the coal tar/water interface changed during coal tar pumping in non-isothermal conditions at $Q=100 \text{ mL}\cdot\text{min}^{-1}$

The fingers are much larger with the coal tar and water liquid pair than with the oil and ethanol model pair. The average and maximum finger length observed for coal tar/water is 0.39 cm and 1.44 cm long. These values are 3 and 2 times higher than observed for oil/ethanol, respectively. However, the same trend was observed: the number and length of the fingers increase up to $t = 30 \text{ min}$ during the formation of the cone of depression, then decrease until the end of the pumping. The fingerings are also larger on the left than on the right. The effect of heating is much more noticeable on fingerings with coal tar/water than for oil/ethanol. The dimensionless numbers and trends with temperature are similar. Thus, the differences in fingering patterns may come from the complexity of coal tar.

7. Conclusions

A 2D-tank experimental setup was designed to reproduce pumping cones of depression for the flow of two immiscible liquids in 1 mm glass beads. The addition of a heating element, similar to those used on real sites, allowed pumping operations to be performed in non-isothermal conditions and the observation of how a pre-heating step influenced the temperature and saturation in the tank.

In isothermal conditions, homogeneous heating improves the efficiency of oil pumping. The residual saturation, estimated by imaging, is decreased from 0.36 to 0.20 by increasing the medium temperature from 20 °C to 32 °C. Then the study of pumping in non-isothermal conditions showed how effective thermal enhancement is to improve the efficiency of oil pumping. Heating reduces the length and number of fingers observed during pumping and improves remediation efficiency.

In non-isothermal conditions, a heating element has been used to generate a temperature field in the 2D tank to reproduce conditions closer to those encountered in a real polluted site. The left part of the cone of depression in the tank, close to the heating element, is thus warmer than the right part. The latter remains close to room temperature. That means that the dynamic viscosity of the oil varies in the tank, unlike the isothermal case where the dynamic viscosity is constant. When pumping in non-isothermal conditions, a slightly unsymmetrical cone forms initially but the final state is symmetrical. We observed that the fingering effects are smaller in the left (heated) part of the cone of depression in the tank than the right. The residual saturation estimated by imaging also follows this pattern:

recovery in non-isothermal conditions is, therefore, more efficient (7% at 20 mL.min⁻¹, 3% at 100 mL.min⁻¹) in the heated parts. Also, we applied a lower flow rate of 20 mL.min⁻¹ in non-isothermal conditions. In this case, a lower number of fingers appeared, and a higher volume of oil (5% more) was recovered from the tank. With an increase in temperature, the critical velocity and the viscosity ratio increased and helped to stabilize the interface between the non-wetting and wetting phase.

We applied these observations to a real pollutant pumping case (coal tar pollution). First, the temperature field is quite different due to the thermal properties of water, which allow better heat transport, especially during the pumping phase. The observation of the fingering changes showed a higher difference in finger length between the left and right parts thanks to the action of the heating before pumping. Unfortunately, the imaging does not allow to obtain coal tar saturation fields due to the excessively high coal tar opacity. However, we could analyze the evolution of the coal tar saturations inside the 2D tank using TDRs sensors.

These experimental measurements have improved the understanding of non-isothermal flows in porous media. They can be used as a basis for the development and validation of a numerical model coupling two-phase flow and heat transfers. This type of model should allow the simulation of the behavior of two immiscible fluids and make prospective analysis prior to remediation processes. For industrial applications, in the case of unfavorable viscosity ratio, this study leads to the recommendation of heating the soil as homogeneously as possible, and then pump at the lower flow rate possible to recover the highest amount of DNAPL possible from the soil.

8. Acknowledgments

This study was performed as part of the “Bioxyval” project. The authors would like to thank ADEME (French Environment and Energy Management Agency) for co-funding the project under the “AMI” program, REMEA, and ANRT for providing the Ph.D. grant for Nicolas Philippe. We thank Ali Irvani and Benjarese Oniangue for their help on experiment measurements. We gratefully acknowledge the financial support provided to the PIVOTS project by the “Région Centre – Val de Loire” and the European Regional Development Fund.

9. References

- Alazaiza, M.Y.D., Ngien, S.K., Bob, M.M., Kamaruddin, S.A., Ishak, W.M.F., 2016. Application of Light Reflection Method to Observe DNAPL Movement in Different Soil Media, in: TheNationalConference Postgraduate Research, Universiti Malaysia Pahang, Pahang, Malaysia.
- Baker, R.S., LaChance, J., Heron, G., 2006. In-pile thermal desorption of PAHs, PCBs and dioxins/furans in soil and sediment. *Land Contamination & Reclamation* 14, 620–624.

- Baston, D.P., Falta, R.W., Kueper, B.H., 2010. Numerical Modeling of Thermal Conductive Heating in Fractured Bedrock. *Ground Water* 48, 836–843.
- Brovelli, A., Cassiani, G., 2008. Effective permittivity of porous media: a critical analysis of the complex refractive index model. *Geophysical Prospecting* 56, 715–727.
- Childs, J., Acosta, E., Annable, M.D., Brooks, M.C., Enfield, C.G., Harwell, J.H., Hasegawa, M., Knox, R.C., Rao, P.S.C., Sabatini, D.A., Shiau, B., Szekeres, E., Wood, A.L., 2006. Field demonstration of surfactant-enhanced solubilization of DNAPL at Dover Air Force Base, Delaware. *Journal of Contaminant Hydrology* 82, 1–22.
- Colombano, S., Davarzani, H., Hullebusch, E.D. van, Huguenot, D., Guyonnet, D., Deparis, J., Ignatiadis, I., 2020. Thermal and chemical enhanced recovery of heavy chlorinated organic compounds in saturated porous media: 1D cell drainage-imbibition experiments. *Science of The Total Environment* 706, 135758.
- Colombano, S., Davarzani, H., Hullebusch, E.D. van, Huguenot, D., Guyonnet, D., Deparis, J., Lion, F., Ignatiadis, I., 2021. Comparison of thermal and chemical enhanced recovery of DNAPL in saturated porous media: 2D tank pumping experiments and two-phase flow modelling. *Science of The Total Environment* 760, 143958.
- Darnault, C.J.G., Throop, J.A., DiCarlo, D.A., Rimmer, A., Steenhuis, T.S., Parlange, J.-Y., 1998. Visualization by light transmission of oil and water contents in transient two-phase flow fields. *Journal of Contaminant Hydrology* 31, 337–348.
- Davarzani, H., Smits, K., Tolene, R.M., Illangasekare, T., 2014. Study of the effect of wind speed on evaporation from soil through integrated modeling of the atmospheric boundary layer and shallow subsurface. *Water Resources Research* 50, 661–680.
- Fitzer, E., Kompalik, D., Yudatet, K., 1987. Rheological characteristics of coal-tar pitches. *Fuel* 66, 1504–1511.
- Gao, B., Davarzani, H., Helmig, R., Smits, K.M., 2018. Experimental and Numerical Study of Evaporation From Wavy Surfaces by Coupling Free Flow and Porous Media Flow. *Water Resources Research* 54, 9096–9117.
- Geel, P.J.V., Sykes, J.F., 1994. Laboratory and model simulations of a LNAPL spill in a variably-saturated sand, 1. Laboratory experiment and image analysis techniques. *Journal of Contaminant Hydrology* 17, 1–25.
- Gerhard, J.I., Kueper, B.H., 2003. Relative permeability characteristics necessary for simulating DNAPL infiltration, redistribution, and immobilization in saturated porous media. *Water Resour. Res.* 39.
- Glass, R.J., Nicholl, M.J., 1996. Physics of gravity fingering of immiscible fluids within porous media: An overview of current understanding and selected complicating factors. *Geoderma* 70, 133–164.
- Hasan, T., Gerhard, J.I., Hadden, R., Rein, G., 2015. Self-sustaining smouldering combustion of coal tar for the remediation of contaminated sand: Two-dimensional experiments and computational simulations. *Fuel* 150, 288–297.
- Heiderscheidt, J.L., Siegrist, R.L., Illangasekare, T.H., 2008. Intermediate-scale 2D experimental investigation of in situ chemical oxidation using potassium permanganate for remediation of complex DNAPL source zones. *Journal of Contaminant Hydrology* 102, 3–16.
- Heron, G., Van Zutphen, M., Christensen, T.H., Enfield, C.G., 1998. Soil Heating for Enhanced Remediation of Chlorinated Solvents: A Laboratory Study on Resistive Heating and Vapor Extraction in a Silty, Low-Permeable Soil Contaminated with Trichloroethylene. *Environ. Sci. Technol.* 32, 1474–1481.
- Iravani, M.A., Deparis, J., Davarzani, H., Colombano, S., Guérin, R., Mainault, A., 2020. The influence of temperature on the dielectric permittivity and complex electrical resistivity of porous media saturated with DNAPLs: A laboratory study. *Journal of Applied Geophysics* 172, 103921.
- Johansson, C., Bataillard, P., Biache, C., Lorgeoux, C., Colombano, S., Joubert, A., Pigot, T., Faure, P., 2019. FerrateVI oxidation of polycyclic aromatic compounds (PAHs and polar PACs) on DNAPL-spiked sand: degradation efficiency and oxygenated by-product formation compared to conventional oxidants. *Environmental Science and Pollution Research*.

- Johnsen, A.R., Wick, L.Y., Harms, H., 2005. Principles of microbial PAH-degradation in soil. *Environmental Pollution* 133, 71–84.
- Johnson, R., Tratnyek, P., Sleep, B., Krol, M., 2011. In Situ Thermal Remediation of DNAPL Source Zones. SERDP Project ER-1458.
- Kavanaugh, M., Kresic, N., 2008. Groundwater Management in Large River Basins, in: M. Dimkic, H.J.B., Kavanaugh, M. (Eds.), IWA Publishing, pp. 520–600.
- Koci, X., Quintard, M., Robin, M., Gabelle, C., 1989. Effet de la température sur les propriétés de déplacement polyphasique en milieux poreux. *Revue de l'Institut français du pétrole* 44, 763–783.
- Krol, M.M., Sleep, B.E., Johnson, R.L., 2011. Impact of low-temperature electrical resistance heating on subsurface flow and transport. *Water Resour. Res.* 47.
- Lee, L.S., Rao, P.S.C., I., O., 1992. Equilibrium partitioning of polycyclic aromatic-hydrocarbons from coal-tar into water. *Environmental Science & Technology*.
- Lenormand, R., Touboul, E., Zarcone, C., 1988. Numerical models and experiments on immiscible displacements in porous media. *Journal of fluid mechanics* 189, 165–187.
- Li, X.D., Schwartz, F.W., 2004. DNAPL remediation with in situ chemical oxidation using potassium permanganate: II. Increasing removal efficiency by dissolving Mn oxide precipitates. *Journal of Contaminant Hydrology* 68, 269–287.
- McDade, J.M., McGuire, T.M., Newell, C.J., 2005. Analysis of DNAPL source-depletion costs at 36 field sites. *Remediation* 15, 9–18.
- Navy, 2008. Plume management zone to manage chlorinated solvents. Naval Weapons Industrial Reserve Plant, Dallas, Texas, USA. Department of the Navy Environmental Restoration Program 2008 progress report, p. 32.
- Newell, C.J., Farhat, S.K., Adamson, D.T., Looney, B.B., 2011. Contaminant Plume Classification System Based on Mass Discharge. *Ground Water* 49, 914–919.
- Pankow, J.F., Cherry, J.A., 1996. Dense chlorinated solvents and other DNAPLs in groundwater: history, behavior, and remediation.
- Philippe, N., Davarzani, H., Colombano, S., Dierick, M., Klein, P.-Y., Marcoux, M., 2020. Experimental study of the temperature effect on two-phase flow properties in highly permeable porous media: Application to the remediation of dense non-aqueous phase liquids (DNAPLs) in polluted soil. *Advances in Water Resources* 146, 103783.
- Rein, G., 2009. Smouldering Combustion Phenomena in Science and Technology.
- Renoldi, F., Lietti L., Saponaro S., Bonomo L., and F.P., 2003. Thermal desorption of a PAH-contaminated soil: a case study. *Ecosystems and Sustainable Development IV Volume 2 WIT Press*, 1123–1132.
- Russell, K.T., Rabideau, A.J., 2000. Decision Analysis for Pump-and-Treat Design. *Ground Water Monitoring & Remediation* 20, 159–168.
- Sanaïotti, G., Silva, C.A.S. da, Parreira, A.G., Tótola, M.R., Meirelles, A.J.A., Batista, E.A.C., 2010. Densities, Viscosities, Interfacial Tensions, and Liquid–Liquid Equilibrium Data for Systems Composed of Soybean Oil + Commercial Linoleic Acid + Ethanol + Water at 298.2 K. *J. Chem. Eng. Data* 55, 5237–5245.
- Scholes, G.C., Gerhard, J.I., Grant, G.P., Major, D.W., Vidumsky, J.E., Switzer, C., Torero, J.L., 2015. Smoldering Remediation of Coal-Tar-Contaminated Soil: Pilot Field Tests of STAR. *Environmental Science & Technology* 49, 14334–14342.
- Switzer, C., Pironi, P., Gerhard, J.I., Rein, G., Torero, J.L., 2009. Self-Sustaining Smoldering Combustion: A Novel Remediation Process for Non-Aqueous-Phase Liquids in Porous Media 43, 5871–5877.
- Tidwell, V.C., Glass, R.J., 1994. X ray and visible light transmission for laboratory measurement of two-dimensional saturation fields in thin-slab systems. *Water Resour. Res.* 30, 2873–2882.
- USEPA, 1996. Pump and Treat Ground Water Remediation A Guide for Decision Makers and Practitioners. EPA/625/R-95/005.
- Wang, J., Dong, M., Asghari, K., 2006. Effect of oil viscosity on heavy oil-water relative permeability curves, in: SPE/DOESymposium Improved Oil Recovery. Society of Petroleum Engineers.

- Wilking, B.T., Rodriguez, D.R., Illangasekare, T.H., 2013. Experimental study of the effects of DNAPL distribution on mass rebound. *Groundwater* 51, 229–236.
- Wu, M., Cheng, Z., Wu, J., Wu, J., 2017. Estimation of representative elementary volume for DNAPL saturation and DNAPL-water interfacial areas in 2D heterogeneous porous media. *Journal of Hydrology* 549, 12–26.

Appendix A. Temperature field during 2D tank heating

Temperature changes are represented in the form of 2D fields via the Surfer software by the kriging method. Figure A. 1 shows the effect of flow rate on the temperature field at the start and end of pumping.

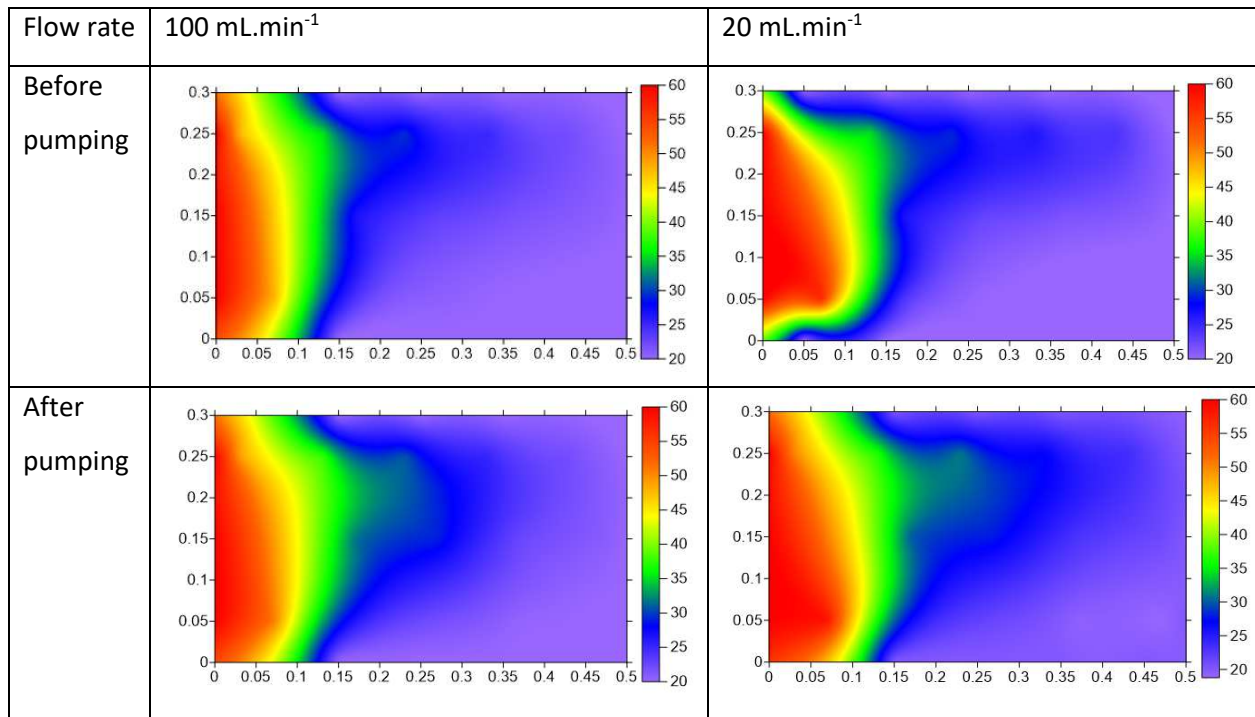


Figure A. 1 Comparison of the temperature fields before and after pumping in non-isothermal conditions for two pumping rates (20 mL.min⁻¹ and 100 mL.min⁻¹)

The temperature is much higher on the left of the tank than on the right in non-isothermal conditions, due to the presence of the heating element. The temperature seems to redirect slightly towards the central and lower part of the tank during pumping for both flow rates, certainly linked to the infiltration of ethanol. The temperature variations occurring during pumping are more easily observed in Figure A. 2, which compares the ratio between temperature measured at the end of pumping divided by the temperature just before pumping ($t = 0$ of pumping).

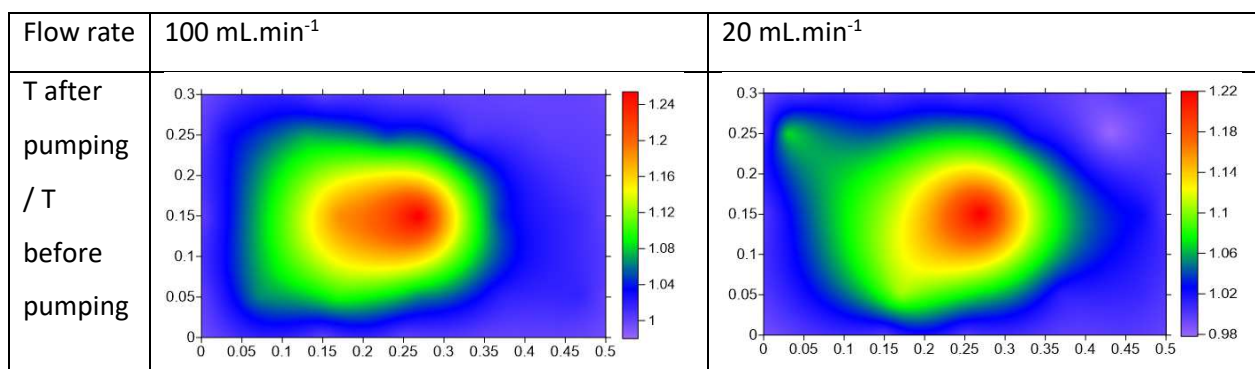


Figure A. 2 Comparison of the ratio between temperature after pumping and initial temperature (before pumping) in non-isothermal conditions for two pumping rates ($20 \text{ mL}\cdot\text{min}^{-1}$ and $100 \text{ mL}\cdot\text{min}^{-1}$)

After pumping, the temperature increases, especially in the center of the tank. This corresponds to the arrival of hot ethanol replacing the oil initially present. At high flow rate, the temperature ratio is substantial in the left and center parts of the tank ($0.05 \text{ m} < x < 0.35 \text{ m}$) due to high convection effects. In conclusion, pumping at a lower flow rate gives a more uniform temperature field, which reduces the viscosity ratio between the oil and ethanol. This effect could translate into a lower residual saturation at lower flow rate.

The temperature fields before and after pumping are shown in Figure A. 3 for the coal tar/water fluid pair.

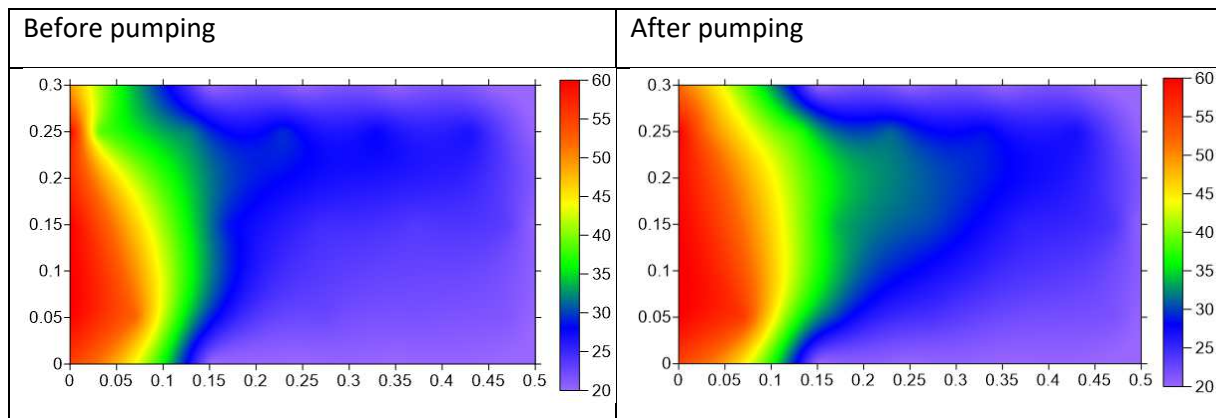


Figure A. 3 Comparison of the temperature fields before ($t = 0 \text{ min}$) and after ($t = 40 \text{ min}$) pumping in non-isothermal conditions for coal tar/water fluids pair

The high temperature is redirected to the central part of the tank during pumping, certainly linked to the infiltration of heated water. Figure A. 4 compares temperature ratio fields between oil/ethanol and coal tar/water pumping cases. The temperature ratio is defined as the temperature after pumping over the initial temperature after heating.

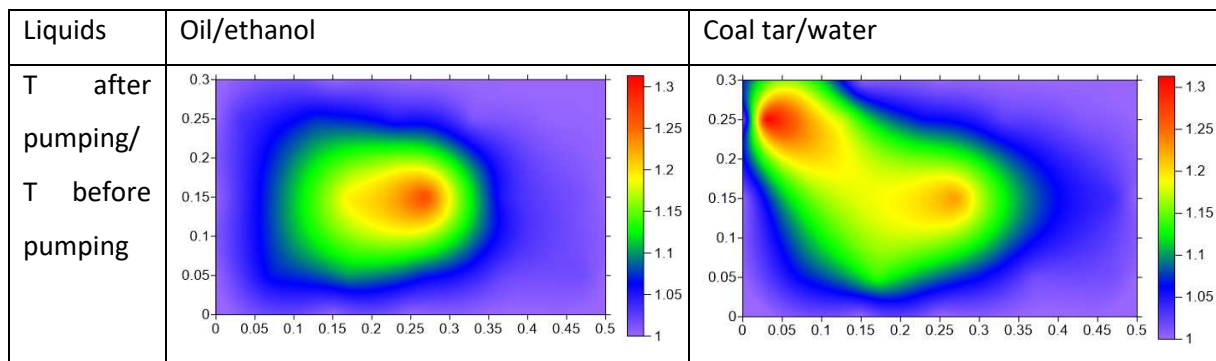


Figure A. 4 Comparison of the ratio between temperature after pumping and initial temperature (before pumping) under non-isothermal conditions for pumping oil at steady state (t = 15 min) and coal tar (t = 40 min); Q = 100 mL.min⁻¹.

The temperature also increases in the upper left part of the coal tar/water case unlike in the oil/ethanol case where most of the pumping increases the temperature in the center of the tank. The thermal conductivity and specific heat capacity of water are higher than those of ethanol. This allows the water to continue heating while pumping.

The calculation of the Reynolds number Re , thermal Péclet number Pe_T , and the Rayleigh number Ra help to understand the heat transfer regimes in non-isothermal conditions. These dimensionless numbers can be calculated as

$$Re = \frac{U_p \ell}{\nu}, \quad Pe_T = \frac{U_p \ell}{\alpha}, \quad Ra = \frac{g\beta(T_h - T_c)KH}{\alpha\nu} \quad (1.A)$$

where T_h (K) and T_c (K) are, respectively, the hot (60 °C) and the cold (20 °C) temperature in the system, β (K⁻¹) is the coefficient of thermal expansion, ℓ (m) characteristic length (solid particle size), H (m) height of liquid in 2D tank, α (m²s⁻¹) thermal diffusivity, ν (m²s⁻¹) kinematic viscosity, and K (m²) intrinsic permeability. The Reynolds and thermal Péclet numbers were calculated using the fluid velocity around the pumping point, U_p . The calculated numbers are listed in Table A. 1.

Table A. 1 dimensionless numbers for different liquid under non-isothermal conditions (Q=100 mL/min)

Liquid	Oil	Ethanol	Coal tar	Water
C_p (Jkg ⁻¹ K ⁻¹)	1840	2420	2100	4180
λ (Wm ⁻¹ K ⁻¹)	1.66×10 ⁻¹	1.68×10 ⁻¹	1.32×10 ⁻¹	5.98×10 ⁻¹
β (K ⁻¹)	5.03×10 ⁻⁴	6.20×10 ⁻⁴	4.82×10 ⁻⁴	2.60×10 ⁻⁴
Re	2.00×10 ⁻³	1.2×10 ⁻¹	6.00×10 ⁻³	2.87×10 ⁻¹
Ra	0.81	62	3.72	37
Pe_T	2.91	3.35	5.02	2.01

The low values of Reynolds number indicate that the flow in porous media can be considered as a creeping flow. The Rayleigh numbers in wetting phases are more than one order of magnitude higher than the ones for non-wetting phases. This indicates that the natural convection should be higher in the upper part of the 2D tank during the heating stage. The Rayleigh number of the saturated ethanol zone is around twice the saturated water zone. The thermal Péclet number of more than one shows that the convection is dominated in all pumping experiments.

Our preliminary simulation of heat transfer during the heating stage shows that the heat loss from 2D tank walls surface is low thanks to the double-walled systems. However, the most important heat loss

can be reproduced from the top surface of the 2D tank which is in direct contact with air circulation inside the fume hood (a coefficient of heat loss around $50-100 \text{ W}\cdot\text{m}^{-2}\cdot\text{K}^{-1}$).